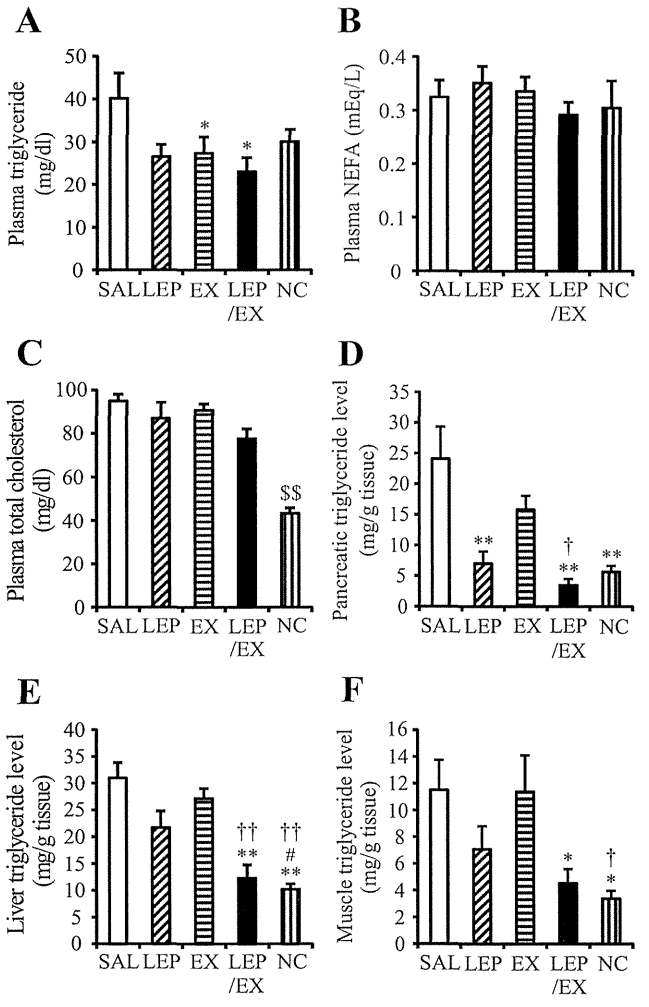

Fig. 2. Effects of leptin and/or exenatide on lipid metabolism in the STZ/HFD mice. *A–C*: plasma triglyceride (*A*), nonesterified fatty acid (NEFA, *B*), and total cholesterol (*C*) levels on *day 14* (n = 12–14 in each infusion group; n = 8 in NC). *D–F*: pancreas (n = 7–10 in each group; *D*), liver (n = 12–14 in each infusion group; n = 8 in NC; *E*), and gastrocnemius muscle (n = 8–9 in each group; *F*) triglyceride levels on *day 14*. Data are reported as means ± SE. $^{*}P < 0.05$ and $^{**}P < 0.01$ vs. SAL. $\#P < 0.05$ vs. LEP. $\dagger P < 0.05$ and $\dagger\dagger P < 0.01$ vs. EX. $\$\$P < 0.01$ for NC vs. the others.

of exenatide in the STZ/HFD mice. However, LEP/EX significantly increased plasma insulin levels at 15 min from those at 0 min (Fig. 1*F*) and markedly augmented the Δinsulin/Δglucose (0–15 min) values than the other three infusion groups (Fig. 1*G*). In IPGTT, at 0 min, the plasma glucose levels were similar among the LEP, EX, and LEP/EX groups. These results suggested that adding leptin to exenatide restored the insulinotropic effect of exenatide in the STZ/HFD mice.

Effects of leptin and/or exenatide on plasma lipid levels and tissue triglyceride levels in the STZ/HFD mice. Because both plasma lipid levels and lipid deposition in the pancreas affect GSIS (22, 41, 45, 50), we measured plasma lipid levels and triglyceride levels in the pancreas.

After the infusion experiment, EX and LEP/EX significantly reduced plasma triglyceride levels, and LEP also tended to reduce comparable to that in the EX and LEP/EX groups (Fig. 2*A*). NEFA and total cholesterol levels remained unchanged (Fig. 2, *B* and *C*). LEP and LEP/EX markedly reduced and almost normalized pancreatic triglyceride levels. Pancreatic triglyceride levels in the LEP/EX group also significantly reduced compared with those in the EX group (Fig. 2*D*). In addition, LEP/EX markedly reduced and almost normalized and LEP tended to reduce triglyceride levels in the liver and skeletal muscle (Fig. 2, *E* and *F*).

Effects of leptin and/or exenatide on food intake, body weight, and energy expenditure in the STZ/HFD mice. Body weight reduction itself may reduce pancreatic triglyceride deposition and improve β-cell function (22, 39). Thus, we examined the effects of leptin and/or exenatide on food intake and body weight in the STZ/HFD mice. Although the body weight was increased in the SAL group during the experiment period, LEP and EX significantly reduced food intake and body weight, and, furthermore, LEP/EX reduced them to a greater extent than either monotherapy (Fig. 3, *A* and *B*). $\dot{V}O_2$ tended to increase in the LEP and LEP/EX groups (Fig. 3*C*). LEP/EX significantly decreased RER, indicating increased utilization of fat as a fuel source (Fig. 3*D*).

PF experiment. Next, we performed a PF experiment to examine the effects of anorexic and weight-reducing effects by LEP/EX on pancreatic triglyceride levels and GSIS. In the PF group, we fed daily the same amount of HFD that was consumed by the LEP/EX group for 14 days to the STZ/HFD mice (Fig. 4*A*). The PF group showed a significant reduction in body

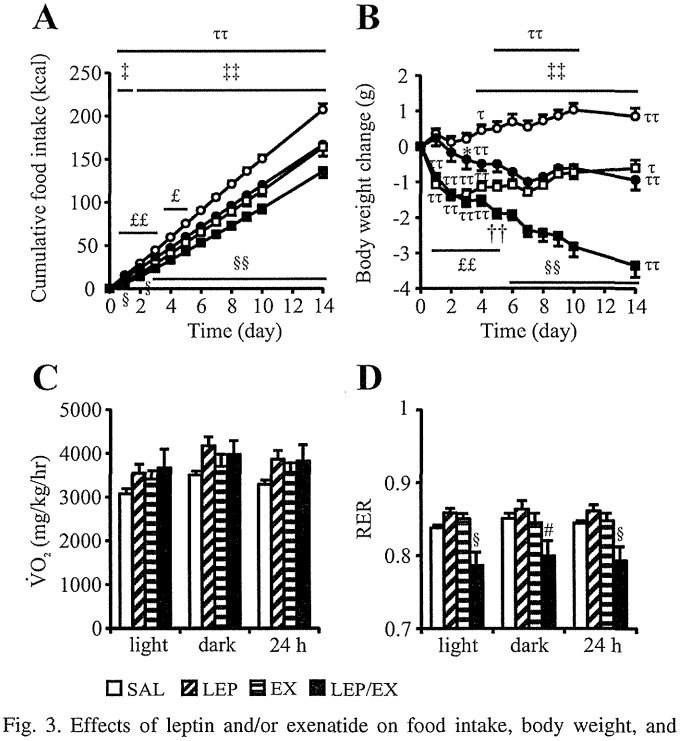

Fig. 3. Effects of leptin and/or exenatide on food intake, body weight, and energy expenditure in the STZ/HFD mice. *A* and *B*: cumulative food intake (*A*) and changes in body weight (*B*) in the SAL (white circles), LEP (black circles), EX (white squares), and LEP/EX (black squares) groups for 14 days (n = 14–18 in each group). *C* and *D*: oxygen consumption ($\dot{V}O_2$, *C*) and respiratory exchange ratio (RER, *D*) on *days 9–10* (n = 4 in each group). Data are reported as means ± SE. Between-group significant differences are indicated at each time point. $^{*}P < 0.05$ vs. SAL. $\#P < 0.05$ vs. LEP. $\dagger\dagger P < 0.01$ vs. EX. $\ddagger P < 0.05$ and $\ddagger\ddagger P < 0.01$ for SAL vs. the others. $\S P < 0.05$ and $\S\S P < 0.01$ for LEP/EX vs. SAL, LEP, and EX. £$P < 0.05$ and ££$P < 0.01$ for EX and LEP/EX vs. SAL and LEP. $\tau P < 0.05$ and $\tau\tau P < 0.01$ vs. the value at *day 0* in the same infusion group.

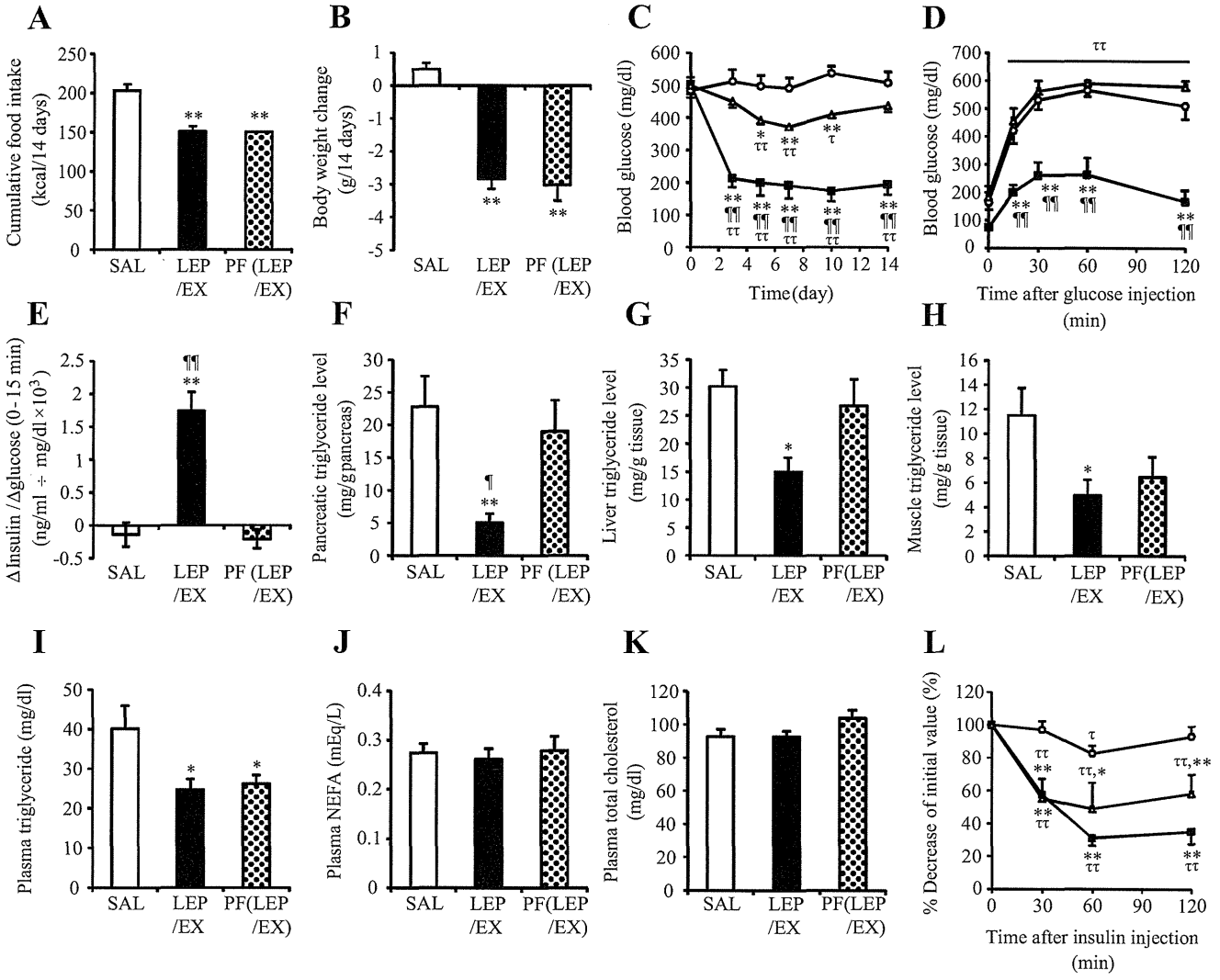

Fig. 4. Pair-feeding experiment. *A* and *B*: cumulative food intake (*A*) and changes in body weight (*B*) for 14 days (n = 11–12 in each group). *C* and *D*: ad libitum blood glucose levels for 14 days (n = 11–12 in each group; *C*) and blood glucose levels during IPGTT (n = 6–7 in each group; *D*) in the SAL (white circles), LEP/EX (black squares), and PF (white triangles) groups. *E*: Δinsulin/Δglucose (0–15 min) values in IPGTT (n = 6–8 in each group). *F–H*: pancreatic (n = 6–8 in each group; *F*), liver (n = 10–11 in each group; *G*), and skeletal muscle (n = 10–12 in each group; *H*) triglyceride levels on *day 14*. *I–K*: plasma triglyceride (*I*), NEFA (*J*), and total cholesterol (*K*) levels on *day 14* (n = 11–12 in each group). *L*: %decrease of initial value of blood glucose levels during ITT in the SAL (white circles), LEP/EX (black squares), and PF (white triangles) groups (n = 6–8 in each group). Data are reported as means ± SE. Between-group significant differences are indicated at each time point. $^{*}P < 0.05$ and $^{**}P < 0.01$ vs. SAL. $\P P < 0.05$ and $\P\P P < 0.01$ vs. PF. $\tau P < 0.05$ and $\tau\tau P < 0.01$ vs. the value at *day 0* or 0 min in the same infusion group.

weight comparable to that in the LEP/EX group (Fig. 4*B*). However, the improvement of blood glucose levels in the PF group was lower than that in the LEP/EX group (Fig. 4*C*). In IPGTT, glucose tolerance did not improve (Fig. 4*D*), and GSIS did not improve in the PF group (Fig. 4*E*). The pancreatic (Fig. 4*F*), liver (Fig. 4*G*), and skeletal muscle (Fig. 4*H*) triglyceride levels were not reduced; plasma lipid levels were comparable to those in the LEP/EX group (Fig. 4, *I*, *J*, and *K*), and the improvement of insulin sensitivity was lower in the PF group than in the LEP/EX group (Fig. 4*L*).

DISCUSSION

In the present study, we used the STZ/HFD mice as a mouse model of type 2 diabetes with increased adiposity. In the mice, adding leptin to exenatide enhanced GSIS to a greater extent than either monotherapy, which was associated with the reduction of pancreatic triglyceride levels. In addition, LEP/EX reduced tissue triglyceride levels in the liver and skeletal muscle, improved insulin sensitivity, and corrected hyperglycemia to a greater extent than either monotherapy. Furthermore, LEP/EX reduced food intake and body weight to a greater extent than either monotherapy. However, the PF experiment indicated that mechanisms other than calorie restriction were involved in the reduction of the pancreatic triglyceride level and the enhancement of GSIS by LEP/EX.

The STZ/HFD mice showed defects in the pancreatic β-cell function (Table 1 and Fig. 1, *F* and *G*) and insulin resistance (Fig. 1*D*). These characteristics are compatible with type 2 diabetes. In addition, plasma leptin levels in the mice (Table 1) suggested that they increased body weight to overweight range because it was reported that twofold increase in plasma leptin levels correspond to a body mass index in the range of 25–30

kg/m^2 in humans (33). Impaired insulin secretion due to STZ injection would have reduced the effect of HFD to increase body weight. Adiposity was also increased in the mice. Therefore, we used the STZ/HFD mice as a mouse model of type 2 diabetes with increased adiposity. Substantially reduced pancreatic insulin levels in the mice (Table 1) also suggested that they were in a late stage of type 2 diabetes. In the mice, LEP/EX markedly improved glucose metabolism.

In healthy individuals, oral glucose ingestion enhances insulin secretion to a greater extent than intravenous glucose infusion (24), which is called the "incretin effect." This effect is elicited by gut hormones such as GLP-1 and glucose-dependent insulinotropic polypeptide (GIP) called "incretin," which are released from the enteroendocrine cells of the intestine in response to meal ingestion (5, 18). However, in patients with type 2 diabetes, the insulinotropic effect of GIP is largely disappeared, and the insulinotropic effect of GLP-1 is also reduced (15, 31). Recent studies have indicated that consequences of the diabetic state, such as reduced β-cell function and mass, could largely contribute to the reduction of the incretin effect in type 2 diabetes, whereas genetic defects (i.e., allelic variation of TCF7L2 and WFS1) and reduced incretin secretion may also contribute (35, 38). Hyperglycemia and hyperlipidemia, which impair β-cell function, can also reduce the incretin effect (15, 50). In this context, Hojberg et al. recently reported that correcting hyperglycemia could restore the insulinotropic effect of GLP-1 (11), and Kang et al. also reported that correcting hyperlipidemia using bezafibrate could restore the insulinotropic effect of exenatide (14). However, in the present study, another factor, besides hyperglycemia and hyperlipidemia, was suspected to play a role in the reduction of the insulinotropic effect of exenatide. Before IPGTT, the blood glucose levels were similar among the LEP, EX, and LEP/EX groups (Fig. 1*E*). Plasma lipid levels were also similar among the three groups (Fig. 2, *A*, *B*, and *C*). However, LEP/EX enhanced GSIS to a greater extent than either monotherapy (Fig. 1*G*).

Pancreatic lipid deposition, which increases with progression of obesity, reportedly causes β-cell dysfunction (41, 45). Improvement of β-cell function associated with the reduction of pancreatic lipid deposition has been found in rodents and humans (22, 39, 46). Even in obese patients with normal glucose tolerance, the pancreatic lipid levels are increased and the incretin effect is reduced (17, 36). These reports had suggested that pancreatic lipid deposition could also affect the incretin effect; however, this has not been confirmed. In the present study, we reported for the first time the restoration of the insulinotropic effect of exenatide by the coadministration of leptin, and this effect was associated with the reduction of pancreatic triglyceride levels in the STZ/HFD mice. (Figs. 1*F*, 1*G*, and 2*D*).

Leptin itself could not be expected to produce direct insulinotropic effects; however, it may improve β-cell functions such as GSIS associated with the reduction of pancreatic lipid deposition in rodents (39, 46). This ectopic lipid-lowering effect of leptin has been reported to be far beyond its effect on food intake and body weight and was attained by mechanisms such as sympathetic nerve activation and increasing lipid oxidation (20, 25, 43). Although a GLP-1 receptor agonist could also reduce ectopic lipid deposition, a substantial effect was associated with body weight reduction (3, 40). The results of the PF experiment also suggested that the reduction of pancreatic triglyceride levels by LEP/EX was achieved by mechanisms other than weight reduction (Fig. 4). Therefore, the marked reduction of pancreatic triglyceride levels by LEP/EX (Fig. 2*D*) could have been achieved by leptin rather than exenatide, at least during the 2 wk of the experimental period. The pancreatic lipid-reducing effect of leptin may have restored β-cell function and the insulinotropic effect of exenatide in the STZ/HFD mice.

There may be some reasons that leptin alone did not restore GSIS, although it did significantly reduce the pancreatic triglyceride levels (Figs. 1*F*, 1*G*, and 2*D*). First, the intrinsic incretin levels may have not been high enough to exert the incretin effect in the LEP group. We performed IPGTT rather than an oral challenge because it enabled the investigation of insulin secretion without any confounding effects from intrinsic incretins. Therefore, incretin levels should have been low in the fasting condition of the LEP group during IPGTT. On the other hand, plasma exenatide levels in the LEP/EX group were 235.7 ± 31.4 pM (Table 2), which was comparable to the plasma GLP-1 level reported in obese patients after undergoing bariatric surgery, and could markedly improve glucose and energy metabolism (8, 21). In addition, in patients with type 2 diabetes, the physiological concentration of GLP-1 could not sufficiently induce GSIS, but a supraphysiological dose of a GLP-1 receptor agonist could; however, compared with healthy controls, the insulinotropic effect of the supraphysiological dose of GLP-1 was still reduced (15, 31). Thus the exenatide treatment may have been necessary to produce a marked restoration of GSIS by LEP/EX in the STZ/HFD mice. Second, the substantial loss of pancreatic β-cells in the STZ/HFD mice, suggested by the reduction of pancreatic insulin levels to less than 1/10th of those of the NC group (Table 1), may have masked the improvement of β-cell function with leptin. Hosokawa et al. reported that GSIS and the insulinotropic effect of GLP-1 were substantially reduced in diabetic rats after a 90% pancreatectomy (12). Thus, leptin alone could not have restored GSIS in the STZ/HFD mice.

Plasma leptin levels in the LEP group (Table 2) were comparable to the peak plasma leptin levels observed in our clinical trial of leptin replacement therapy in patients with lipodystrophy (6), and it could be clinically applicable in humans.

The anorexic and weight-reducing effects of leptin and GLP-1 are reduced in obesity (1, 4, 9, 44). However, LEP/EX enhanced these effects to a greater extent than either monotherapy (Fig. 3, *A* and *B*). These results were similar to those recent reports by Williams and others using lean and obese rodents (27, 48). As for mechanisms, Williams et al. reported that leptin could potentiate the anorexic effect of GLP-1 via central nervous system (CNS) mechanisms (48). On the other hand, the marked reduction of tissue triglyceride levels (Fig. 2, *D*, *E*, and *F*) and RER (Fig. 3*D*) by LEP/EX also suggested the action of leptin being restored because these effects were expected with leptin rather than exenatide (2, 3). GLP-1 could also regulate glucose metabolism via CNS mechanisms such as the arcuate nucleus in the hypothalamus, which plays an essential role in the glucoregulatory action of leptin (16, 37). Thus, leptin and exenatide may have interacted to restore each other's energy balance regulating and glucoregulatory effects via CNS mechanisms. This issue may also have a therapeutic

potential but requires further investigation. Furthermore, the STZ/HFD mice would not be obese but overweight as mentioned above, and the glucose-lowering effect of leptin monotherapy was partially preserved in the present study. Whether LEP/EX could exhibit marked glucose-lowering effect to a greater extent than either monotherapy even in leptin-resistant (9) obese type 2 diabetes will deserve specific attention in the future.

In conclusion, our findings suggest that leptin treatment may restore the insulinotropic effect of exenatide associated with the reduction of the pancreatic lipid deposition in type 2 diabetes with increased adiposity. In addition, the coadministration of leptin and exenatide reduced food intake and body weight to a greater extent than either monotherapy. Thus, combination therapy with leptin and exenatide could be an effective treatment for patients with type 2 diabetes with increased adiposity.

ACKNOWLEDGMENTS

We thank Mayumi Nagamoto for technical assistance and Yoko Koyama for secretarial assistance.

GRANTS

This work was supported in part by research grants from JSPS KAKENHI (Grant No. 23791054); the Ministry of Education, Culture, Sports, Science and Technology of Japan, including a Grant-in-Aid for Scientific Research on Innovative Areas (Research in a proposed research area) "Molecular Basis and Disorders of Control of Appetite and Fat Accumulation"; the Ministry of Health, Labour and Welfare of Japan; Japan Foundation for Applied Enzymology; the Takeda Medical Research Foundation; the Smoking Research Foundation; Suzuken Memorial Foundation; Novo Nordisk Insulin Research award; and Lilly Education and Research Grant Office.

DISCLOSURES

No conflicts of interest, financial or otherwise, are declared by the authors.

AUTHOR CONTRIBUTIONS

Author contributions: T.S., T.K., K.E., and K.N. conception and design of research; T.S. performed experiments; T.S. analyzed data; T.S., T.K., K.E., D.A., S.Y.-K., Z.M., V.M.J.G., C.E., M.A.-A., Y.Y., M.N., J.F., K.H., N.I., and K.N. interpreted results of experiments; T.S. prepared figures; T.S. drafted manuscript; T.S., T.K., and K.N. approved final version of manuscript; T.K., K.E., N.I., and K.N. edited and revised manuscript.

REFERENCES

1. **Aotani D, Ebihara K, Sawamoto N, Kusakabe T, Aizawa-Abe M, Kataoka S, Sakai T, Iogawa H, Ebihara C, Fujikura J, Hosoda K, Fukuyama H, Nakao K.** Functional magnetic resonance imaging analysis of food-related brain activity in patients with lipodystrophy undergoing leptin replacement therapy. *J Clin Endocrinol Metab* 97: 3663–3671, 2012.
2. **Bradley DP, Kulstad R, Racine N, Shenker Y, Meredith M, Schoeller DA.** Alterations in energy balance following exenatide administration. *Appl Physiol Nutr Metab* 37: 893–899, 2012.
3. **Cummings BP, Stanhope KL, Graham JL, Baskin DG, Griffen SC, Nilsson C, Sams A, Knudsen LB, Raun K, Havel PJ.** Chronic administration of the glucagon-like peptide-1 analog, liraglutide, delays the onset of diabetes and lowers triglycerides in UCD-T2DM rats. *Diabetes* 59: 2653–2661, 2010.
4. **Duca FA, Sakar Y, Covasa M.** Combination of obesity and high-fat feeding diminishes sensitivity to GLP-1R agonist exendin-4. *Diabetes* 62: 2410–2415, 2013.
5. **Dupre J, Ross SA, Watson D, Brown JC.** Stimulation of insulin secretion by gastric inhibitory polypeptide in man. *J Clin Endocrinol Metab* 37: 5: 826–828, 1973.
6. **Ebihara K, Kusakabe T, Hirata M, Masuzaki H, Miyanaga F, Kobayashi N, Tanaka T, Chusho H, Miyazawa T, Hayashi T, Hosoda K, Ogawa Y, DePaoli AM, Fukushima M, Nakao K.** Efficacy and safety of leptin-replacement therapy and possible mechanisms of leptin actions in patients with generalized lipodystrophy. *J Clin Endocrinol Metab* 92: 532–541, 2007.
7. **Ebihara K, Ogawa Y, Masuzaki H, Shintani M, Miyanaga F, Aizawa-Abe M, Hayashi T, Hosoda K, Inoue G, Yoshimasa Y, Gavrilova O, Reitman ML, Nakao K.** Transgenic overexpression of leptin rescues insulin resistance and diabetes in a mouse model of lipoatrophic diabetes. *Diabetes* 50: 1440–1448, 2001.
8. **Goldfine AB, Mun EC, Devine E, Bernier R, Baz-Hecht M, Jones DB, Schneider BE, Holst JJ, Patti ME.** Patients with neuroglycopenia after gastric bypass surgery have exaggerated incretin and insulin secretory responses to a mixed meal. *J Clin Endocrinol Metab* 92: 4678–4685, 2007.
9. **Heymsfield SB, Greenberg AS, Fujioka K, Dixon RM, Kushner R, Hunt T, Lubina JA, Patane J, Self B, Hunt P, McCamish M.** Recombinant leptin for weight loss in obese and lean adults: a randomized, controlled, dose-escalation trial. *J Am Med Assoc* 282: 1568–1575, 1999.
10. **Hodson DJ, Mitchell RK, Bellomo EA, Sun G, Vinet L, Meda P, Li D, Li WH, Bugliani M, Marchetti P, Bosco D, Piemonti L, Johnson P, Hughes SJ, Rutter GA.** Lipotoxicity disrupts incretin-regulated human beta cell connectivity. *J Clin Invest* 123: 4182–4194, 2013.
11. **Hojberg PV, Vilsboll T, Rabol R, Knop FK, Bache M, Krarup T, Holst JJ, Madsbad S.** Four weeks of near-normalisation of blood glucose improves the insulin response to glucagon-like peptide-1 and glucose-dependent insulinotropic polypeptide in patients with type 2 diabetes. *Diabetologia* 52: 199–207, 2009.
12. **Hosokawa YA, Hosokawa H, Chen C, Leahy JL.** Mechanism of impaired glucose-potentiated insulin secretion in diabetic 90% pancreatectomy rats. Study using glucagon-like peptide-1 (7–37). *J Clin Invest* 97: 180–186, 1996.
13. **Kamohara S, Burcelin R, Halaas JL, Friedman JM, Charron MJ.** Acute stimulation of glucose metabolism in mice by leptin treatment. *Nature* 389: 374–377, 1997.
14. **Kang ZF, Deng Y, Zhou Y, Fan RR, Chan JC, Laybutt DR, Luzuriaga J, Xu G.** Pharmacological reduction of NEFA restores the efficacy of incretin-based therapies through GLP-1 receptor signalling in the beta cell in mouse models of diabetes. *Diabetologia* 56: 423–433, 2013.
15. **Kjems LL, Holst JJ, Volund A, Madsbad S.** The influence of GLP-1 on glucose-stimulated insulin secretion: effects on beta-cell sensitivity in type 2 and nondiabetic subjects. *Diabetes* 52: 380–386, 2003.
16. **Knauf C, Cani PD, Perrin C, Iglesias MA, Maury JF, Bernard E, Benhamed F, Gremeaux T, Drucker DJ, Kahn CR, Girard J, Tanti JF, Delzenne NM, Postic C, Burcelin R.** Brain glucagon-like peptide-1 increases insulin secretion and muscle insulin resistance to favor hepatic glycogen storage. *J Clin Invest* 115: 3554–3563, 2005.
17. **Knop FK, Aaboe K, Vilsboll T, Volund A, Holst JJ, Krarup T, Madsbad S.** Impaired incretin effect and fasting hyperglucagonaemia characterizing type 2 diabetic subjects are early signs of dysmetabolism in obesity. *Diabetes Obes Metab* 14: 500–510, 2012.
18. **Kreymann B, Williams G, Ghatei MA, Bloom SR.** Glucagon-like peptide-1 7–36: a physiological incretin in man. *Lancet* 2: 8571: 1300–1304, 1987.
19. **Kusakabe T, Ebihara K, Sakai T, Miyamoto L, Aotani D, Yamamoto Y, Yamamoto-Kataoka S, Aizawa-Abe M, Fujikura J, Hosoda K, Nakao K.** Amylin improves the effect of leptin on insulin sensitivity in leptin-resistant diet-induced obese mice. *Am J Physiol Endocrinol Metab* 302: E924–E931, 2012.
20. **Kusakabe T, Tanioka H, Ebihara K, Hirata M, Miyamoto L, Miyanaga F, Hige H, Aotani D, Fujisawa T, Masuzaki H, Hosoda K, Nakao K.** Beneficial effects of leptin on glycaemic and lipid control in a mouse model of type 2 diabetes with increased adiposity induced by streptozotocin and a high-fat diet. *Diabetologia* 52: 675–683, 2009.
21. **Laferrere B, Teixeira J, McGinty J, Tran H, Egger JR, Colarusso A, Kovack B, Bawa B, Koshy N, Lee H, Yapp K, Olivan B.** Effect of weight loss by gastric bypass surgery versus hypocaloric diet on glucose and incretin levels in patients with type 2 diabetes. *J Clin Endocrinol Metab* 93: 2479–2485, 2008.
22. **Lim EL, Hollingsworth KG, Aribisala BS, Chen MJ, Mathers JC, Taylor R.** Reversal of type 2 diabetes: normalisation of beta cell function in association with decreased pancreas and liver triacylglycerol. *Diabetologia* 54: 2506–2514, 2011.
23. **Masuzaki H, Ogawa Y, Aizawa-Abe M, Hosoda K, Suga J, Ebihara K, Satoh N, Iwai H, Inoue G, Nishimura H, Yoshimasa Y, Nakao K.** Glucose metabolism and insulin sensitivity in transgenic mice overex-

pressing leptin with lethal yellow agouti mutation: usefulness of leptin for the treatment of obesity-associated diabetes. *Diabetes* 48: 1615–1622, 1999.

24. **McIntyr EN, Holdsworth CD, Turner DS.** New interpretation of oral glucose tolerance. *Lancet* 2: 20–21, 1964.
25. **Miyamoto L, Ebihara K, Kusakabe T, Aotani D, Yamamoto-Kataoka S, Sakai T, Aizawa-Abe M, Yamamoto Y, Fujikura J, Hayashi T, Hosoda K, Nakao K.** Leptin activates hepatic 5′-AMP-activated protein kinase through sympathetic nervous system and alpha1-adrenergic receptor: a potential mechanism for improvement of fatty liver in lipodystrophy by leptin. *J Biol Chem* 287: 40441–40447, 2012.
26. **Miyanaga F, Ogawa Y, Ebihara K, Hidaka S, Tanaka T, Hayashi S, Masuzaki H, Nakao K.** Leptin as an adjunct of insulin therapy in insulin-deficient diabetes. *Diabetologia* 46: 1329–1337, 2003.
27. **Muller TD, Sullivan LM, Habegger K, Yi CX, Kabra D, Grant E, Ottaway N, Krishna R, Holland J, Hembree J, Perez-Tilve D, Pfluger PT, DeGuzman MJ, Siladi ME, Kraynov VS, Axelrod DW, DiMarchi R, Pinkstaff JK, Tschop MH.** Restoration of leptin responsiveness in diet-induced obese mice using an optimized leptin analog in combination with exendin-4 or FGF21. *J Pept Sci* 18: 383–393, 2012.
28. **Naito M, Fujikura J, Ebihara K, Miyanaga F, Yokoi H, Kusakabe T, Yamamoto Y, Son C, Mukoyama M, Hosoda K, Nakao K.** Therapeutic impact of leptin on diabetes, diabetic complications, and longevity in insulin-deficient diabetic mice. *Diabetes* 60: 2265–2273, 2011.
29. **Nauck M, Stockmann F, Ebert R, Creutzfeldt W.** Reduced incretin effect in type 2 (non-insulin-dependent) diabetes. *Diabetologia* 29: 46–52, 1986.
30. **Nauck MA, El-Ouaghlidi A, Gabrys B, Hucking K, Holst JJ, Deacon CF, Gallwitz B, Schmidt WE, Meier JJ.** Secretion of incretin hormones (GIP and GLP-1) and incretin effect after oral glucose in first-degree relatives of patients with type 2 diabetes. *Regul Pept* 122: 209–217, 2004.
31. **Nauck MA, Heimesaat MM, Orskov C, Holst JJ, Ebert R, Creutzfeldt W.** Preserved incretin activity of glucagon-like peptide 1 [7–36 amide] but not of synthetic human gastric inhibitory polypeptide in patients with type-2 diabetes mellitus. *J Clin Invest* 91: 301–307, 1993.
32. **Ogawa Y, Masuzaki H, Hosoda K, Aizawa-Abe M, Suga J, Suda M, Ebihara K, Iwai H, Matsuoka N, Satoh N, Odaka H, Kasuga H, Fujisawa Y, Inoue G, Nishimura H, Yoshimasa Y, Nakao K.** Increased glucose metabolism and insulin sensitivity in transgenic skinny mice overexpressing leptin. *Diabetes* 48: 1822–1829, 1999.
33. **Peltz G, Sanderson M, Perez A, Sexton K, Ochoa Casares D, Fadden MK.** Serum leptin concentration, adiposity, and body fat distribution in Mexican-Americans. *Arch Med Res* 38: 5: 563–570, 2007.
34. **Perry RJ, Zhang XM, Zhang D, Kumashiro N, Camporez JP, Cline GW, Rothman DL, Shulman GI.** Leptin reverses diabetes by suppression of the hypothalamic-pituitary-adrenal axis. *Nat Med* 20: 7: 759–763, 2014.
35. **Pilgaard K, Jensen CB, Schou JH, Lyssenko V, Wegner L, Brons C, Vilsboll T, Hansen T, Madsbad S, Holst JJ, Volund A, Poulsen P, Groop L, Pedersen O, Vaag AA.** The T allele of rs7903146 TCF7L2 is associated with impaired insulinotropic action of incretin hormones, reduced 24 h profiles of plasma insulin and glucagon, and increased hepatic glucose production in young healthy men. *Diabetologia* 52: 1298–1307, 2009.
36. **Saisho Y, Butler AE, Meier JJ, Monchamp T, Allen-Auerbach M, Rizza RA, Butler PC.** Pancreas volumes in humans from birth to age one hundred taking into account sex, obesity, and presence of type-2 diabetes. *Clin Anat* 20: 933–942, 2007.
37. **Sandoval DA, Bagnol D, Woods SC, D'Alessio DA, Seeley RJ.** Arcuate glucagon-like peptide 1 receptors regulate glucose homeostasis but not food intake. *Diabetes* 57: 2046–2054, 2008.
38. **Schafer SA, Mussig K, Staiger H, Machicao F, Stefan N, Gallwitz B, Haring HU, Fritsche A.** A common genetic variant in WFS1 determines impaired glucagon-like peptide-1-induced insulin secretion. *Diabetologia* 52: 1075–1082, 2009.
39. **Shimabukuro M, Koyama K, Chen G, Wang MY, Trieu F, Lee Y, Newgard CB, Unger RH.** Direct antidiabetic effect of leptin through triglyceride depletion of tissues. *Proc Natl Acad Sci USA* 94: 4637–4641, 1997.
40. **Sorhede Winzell M, Ahren B.** Glucagon-like peptide-1 and islet lipolysis. *Horm Metab Res* 36: 795–803, 2004.
41. **Szczepaniak LS, Victor RG, Mathur R, Nelson MD, Szczepaniak EW, Tyer N, Chen I, Unger RH, Bergman RN, Lingvay I.** Pancreatic steatosis and its relationship to beta-cell dysfunction in humans: racial and ethnic variations. *Diabetes Care* 35: 2377–2383, 2012.
42. **Tamura Y, Tanaka Y, Sato F, Choi JB, Watada H, Niwa M, Kinoshita J, Ooka A, Kumashiro N, Igarashi Y, Kyogoku S, Maehara T, Kawasumi M, Hirose T, Kawamori R.** Effects of diet and exercise on muscle and liver intracellular lipid contents and insulin sensitivity in type 2 diabetic patients. *J Clin Endocrinol Metab* 90: 3191–3196, 2005.
43. **Tanaka T, Hidaka S, Masuzaki H, Yasue S, Minokoshi Y, Ebihara K, Chusho H, Ogawa Y, Toyoda T, Sato K, Miyanaga F, Fujimoto M, Tomita T, Kusakabe T, Kobayashi N, Tanioka H, Hayashi T, Hosoda K, Yoshimatsu H, Sakata T, Nakao K.** Skeletal muscle AMP-activated protein kinase phosphorylation parallels metabolic phenotype in leptin transgenic mice under dietary modification. *Diabetes* 54: 2365–2374, 2005.
44. **Turton MD, O'Shea D, Gunn I, Beak SA, Edwards CM, Meeran K, Choi SJ, Taylor GM, Heath MM, Lambert PD, Wilding JP, Smith DM, Ghatei MA, Herbert J, Bloom SR.** A role for glucagon-like peptide-1 in the central regulation of feeding. *Nature* 379: 69–72, 1996.
45. **Tushuizen ME, Bunck MC, Pouwels PJ, Bontemps S, van Waesberghe JH, Schindhelm RK, Mari A, Heine RJ, Diamant M.** Pancreatic fat content and beta-cell function in men with and without type 2 diabetes. *Diabetes Care* 30: 2916–2921, 2007.
46. **Wang MY, Koyama K, Shimabukuro M, Mangelsdorf D, Newgard CB, Unger RH.** Overexpression of leptin receptors in pancreatic islets of Zucker diabetic fatty rats restores GLUT-2, glucokinase, and glucose-stimulated insulin secretion. *Proc Natl Acad Sci USA* 95: 11921–11926, 1998.
47. **Wang MY, Chen L, Clark GO, Lee Y, Stevens RD, Ilkayeva OR, Wenner BR, Bain JR, Charron MJ, Newgard CB, Unger RH.** Leptin therapy in insulin-deficient type I diabetes. *Proc Natl Acad Sci USA* 107: 4813–4819, 2010.
48. **Williams DL, Baskin DG, Schwartz MW.** Leptin regulation of the anorexic response to glucagon-like peptide-1 receptor stimulation. *Diabetes* 55: 3387–3393, 2006.
49. **Xu G, Kaneto H, Laybutt DR, Duvivier-Kali VF, Trivedi N, Suzuma K, King GL, Weir GC, Bonner-Weir S.** Downregulation of GLP-1 and GIP receptor expression by hyperglycemia: possible contribution to impaired incretin effects in diabetes. *Diabetes* 56: 1551–1558, 2007.
50. **Zhou YP, Grill VE.** Long-term exposure of rat pancreatic islets to fatty acids inhibits glucose-induced insulin secretion and biosynthesis through a glucose fatty acid cycle. *J Clin Invest* 93: 870–876, 1994.

SCIENTIFIC REPORTS

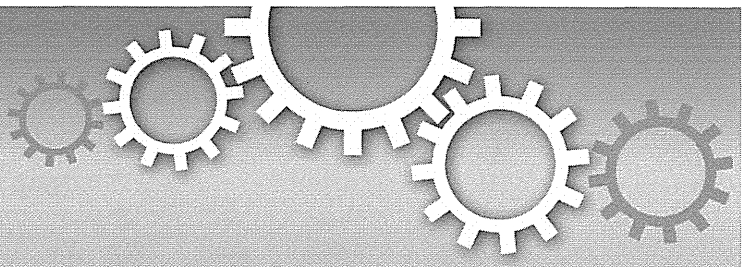

OPEN

SUBJECT AREAS:
GENE REGULATION
CARDIOMYOPATHIES
DNA RECOMBINATION
CYTOGENETICS

Received
28 August 2014

Accepted
12 December 2014

Published
16 January 2015

Correspondence and requests for materials should be addressed to T.N. (takuro-ind@umin.net)

Somatic chromosomal translocation between *Ewsr1* and *Fli1* loci leads to dilated cardiomyopathy in a mouse model

Miwa Tanaka[1], Shuichi Yamaguchi[1], Yukari Yamazaki[1], Hideyuki Kinoshita[2], Koichiro Kuwahara[2], Kazuwa Nakao[2], Patrick Y. Jay[3], Tetsuo Noda[4] & Takuro Nakamura[1]

[1]Division of Carcinogenesis, The Cancer Institute, Japanese Foundation for Cancer Research, 3-8-31 Ariake, Koto-ku, Tokyo 135-8550, Japan, [2]Department of Cardiovascular Medicine, Kyoto University Graduate School of Medicine, 54 Kawaracho Shogoin, Sakyo-ku, Kyoto 606-8507, Japan, [3]Departments of Pediatrics and Genetics, Washington University School of Medicine, 660 S Euclid Avenue, St. Louis, MO 63110, U.S.A, [4]Division of Cell Biology, The Cancer Institute, Japanese Foundation for Cancer Research, 3-8-31 Ariake, Koto-ku, Tokyo 135-8550, Japan.

A mouse model that recapitulates the human Ewing's sarcoma-specific chromosomal translocation was generated utilizing the *Cre/lox*P-mediated recombination technique. A cross between *Ewsr1-lox*P and *Fli1-lox*P mice and expression of ubiquitous Cre recombinase induced a specific translocation between *Ewsr1* and *Fli1* loci in systemic organs of both adult mice and embryos. As a result *Ewsr1-Fli1* fusion transcripts were expressed, suggesting a functional Ews-Fli1 protein might be synthesized *in vivo*. However, by two years of age, none of the *Ewsr1*-loxP/*Fli1*-loxP/CAG-Cre (EFCC) mice developed any malignancies, including Ewing-like small round cell sarcoma. Unexpectedly, all the EFCC mice suffered from dilated cardiomyopathy and died of chronic cardiac failure. Genetic recombination between *Ewsr1* and *Fli1* was confirmed in the myocardial tissue and apoptotic cell death of cardiac myocytes was observed at significantly higher frequency in EFCC mice. Moreover, expression of *Ews-Fli1* in the cultured cardiac myocytes induced apoptosis. Collectively, these results indicated that ectopic expression of the *Ews-Fli1* oncogene stimulated apoptotic signals, and suggested an important relationship between oncogenic signals and cellular context in the cell-of-origin of Ewing's sarcoma.

Chromosomal translocation is a common feature of malignant neoplasms[1]. There is growing evidence that tumor-specific translocations and inversions commonly occur among hematopoietic, mesenchymal and epithelial tumors. An increasing number of gene fusions resulting from translocation have been observed as novel technological tools have been applied. Tumor-associated chromosomal translocations include two major molecular mechanisms. One is an oncogene juxtaposition to the enhancing elements of immunoglobulin or T-cell receptor associated with lymphoid neoplasms. As a result of the juxtaposition, constitutive expression of oncogenes such as *c-MYC, BCL2* or *CCND1* induces abnormal cellular functions, including cell cycle progression and apoptosis suppression[1]. Another important outcome of translocation in cancer is gene fusion or formation of chimeric genes. Two major functional aberrations of fusion gene products are constitutive activation of signal transduction and dysregulation of transcription. Most oncogenic gene fusions in human bone and soft tissue sarcomas belong to the latter group, and there is a specific relationship between tumor types and each gene fusion[2].

To clarify the functional roles of sarcoma-specific chromosomal translocations and gene fusions, it would be ideal to induce chromosomal translocation in animal models *in vivo*. In contrast to transgenic expression of fusion genes, translocation-mediated gene fusion recapitulates gene expression levels equivalent to, and splice variants similar to those in human tumors. Inducible, site-specific chromosomal translocation has been achieved using Cre-*lox*P-mediated recombination in murine ES cells. Using this strategy, translocations between c-myc and immunoglobulin heavy chain loci, and between *Dek* and *Can* loci were successfully induced, though the efficiencies were not very high[3,4]. Indeed, a mouse model of Cre-*lox*P-mediated *in vivo* gene fusion between *Mll* and *Af9* developed acute myeloid leukemia[5]. However, it is not known whether solid tumor-related translocation *in vivo* can induce malignancies of the anticipated phenotypes.

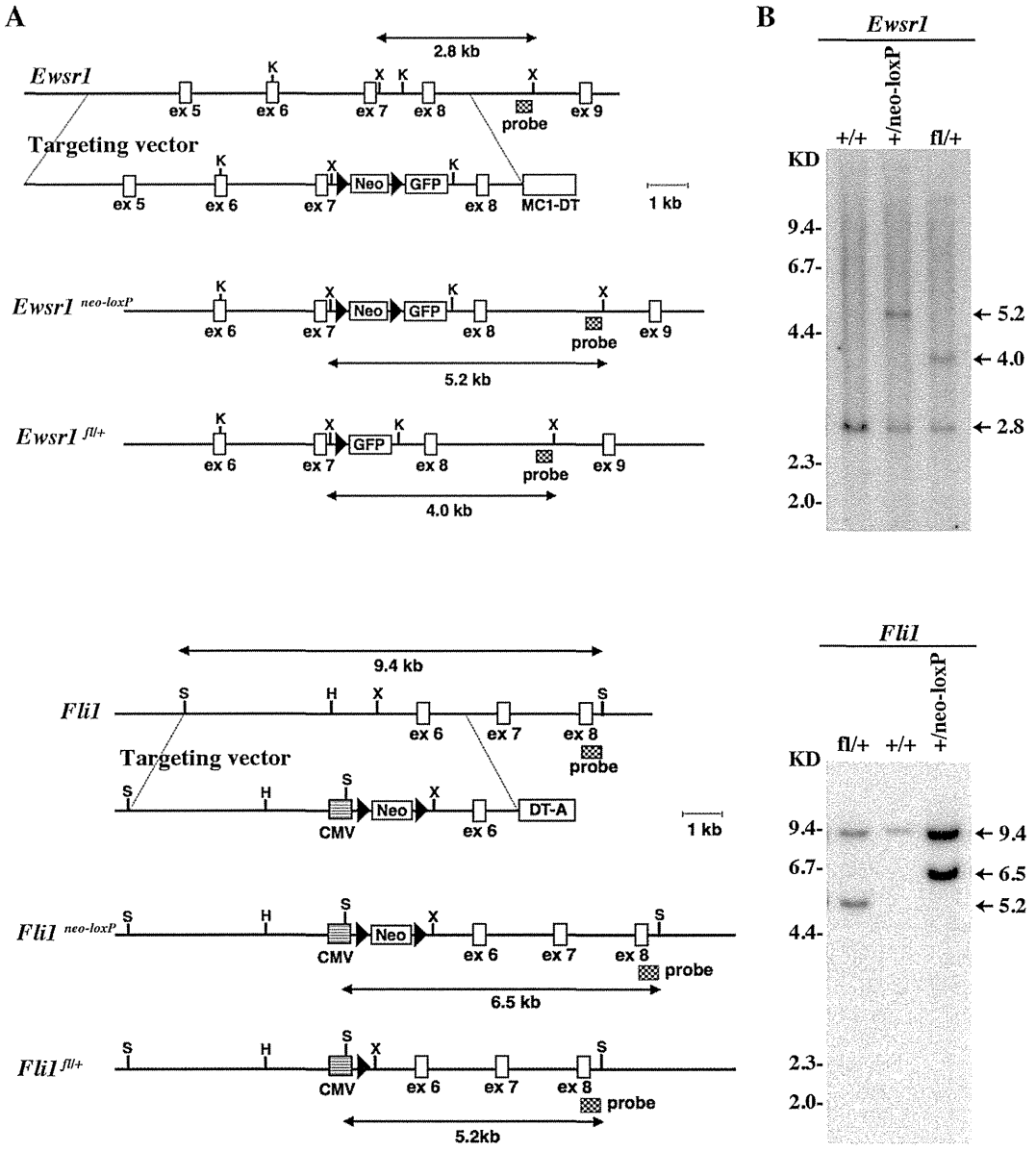

Figure 1 | Gene targeting for the *Ewsr1-Fli1* translocation model. (A) Physical maps of targeting alleles for *Ewsr1* (top) and *Fli1* (bottom) loci. Closed triangles indicate the *lox*P sequence. K: *Kpn*I, X: *Xba*I, S: *Sac*I, H: *Hin*dIII. (B) Southern blot analysis of ES cells. A 5.2 kb *Neo*-positive band and a 4.0 kb *Neo*-deleted band indicate homologous recombination of the *Ewsr1* locus as shown by *Xba*I digestion (top). A 6.5 kb *Neo*-positive band and a 5.2 kb *Neo*-deleted bands for the *Fli1* locus are shown by *Sac*I digestion (bottom). Rearranged bands are indicated by arrows.

The ETS family of transcription factors includes FLI1 and ERG. They are major fusion partners for the *EWSR1* gene in human Ewing's sarcoma[6,7]. EWS-FLI1 and EWS-ERG function as oncogenic transcription factors that dysregulate their downstream targets such as *NKX2-2*, *NR0B1* and *EZH2*[8]. It is, however, difficult to generate a good animal model by introduction of *EWS-FLI1* or *EWS-ERG* into ES cells or mouse eggs[8]. Moreover, conditional *EWS-FLI1* expression in hematopoietic cells induced myeloid and erythroid leukemia in mice[9]. Thus, it might be necessary to activate multiple target genes without activating pro-apoptosis signals for tumorigenic activity of EWS-ETS. We therefore hypothesized that EWS-ETS translocation is achieved by chance in human somatic cells of appropriate lineages and differentiation status, and such *in vivo* translocation could properly induce Ewing's sarcoma.

In an effort to induce Ewing's sarcoma in a mouse model, we have succeeded in promoting *in vivo* Cre-*lox*P-mediated translocation between *Ewsr1* and *Fli1* loci on chromosomes 11 and 9, respectively. Although the *Ewsr1-Fli1* fusion was confirmed at both DNA and RNA levels, no neoplastic lesion was induced in the model. Unexpectedly, the mice with systemic translocation developed dilated cardiomyopathy due to degeneration and apoptotic cell death of cardiac myocytes. The result indicates that ectopic chromosomal translocation and gene fusion activates apoptotic signals, resulting in degenerative cardiac disease.

Results

Generation of a mouse model for somatic chromosomal translocation between *Ewsr1* and *Fli1*. To induce locus-specific chromosomal translocation, *lox*P sequences were introduced into *Ewsr1* intron 7 on mouse chromosome 11 and *Fli1* intron 5 on chromosome 9 (Fig. 1A), since chromosomal breakpoints in human Ewing's sarcoma are most frequently observed in these loci[10]. Successful

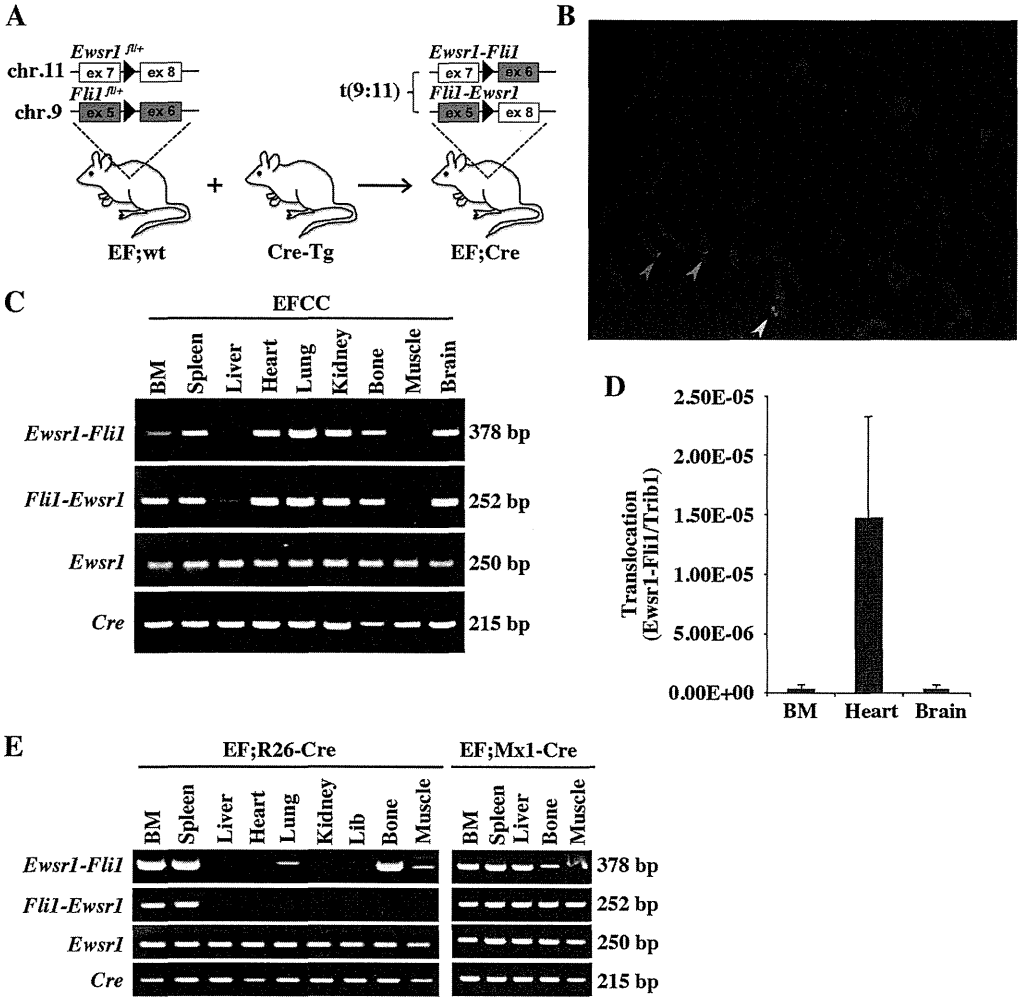

Figure 2 | Somatic chromosomal translocation between mouse chromosomes 9 and 11. (A) A schematic diagram of the *Cre*-mediated translocation model. EF;wt, *Ewsr1*$^{fl/+}$:*Fli1*$^{fl/+}$:wild-type. Cre-Tg, *Cre* transgenic. EF;Cre, *Ewsr1*$^{fl/+}$:*Fli1*$^{fl/+}$: *Cre* transgenic. Illustration of mice was drawn using Microsoft PowerPoint 2011 and then converted to tif format using Adobe Photoshop CS5. (B) Metaphase FISH shows t(9;11) translocation at *Ewsr1* and *Fli1* loci. The green fluorescence of 64E17 shows *Ewsr1* on chromosome 11 and the red fluorescence of 218O21 shows *Fli1* on chromosome 9. The yellow signal indicates translocation between two loci on *der9*. (C) The reciprocal t(9;11) translocation was shown in systemic organs of the EFCC mouse detected as *Ewsr1-Fli1* and *Fli1-Ewsr1* PCR products. *Ewsr1* amplification is shown as a loading control. (D) Estimated frequencies of translocation in bone marrow (BM), heart and brain calculated from the result of quantitative genomic PCR data in three independent mouse samples. (E) The reciprocal t(9;11) translocation in the organs of *Rosa26-CreER* and *Mx1-Cre* background detected by nested genomic PCR. Gel image shown is cropped and representative of gels run under the same experimental conditions.

knock-in of *lox*P sequences mediated by homologous recombination was confirmed for both loci in independent ES cells by Southern blotting (Fig. 1B). Both *Ewsr1*$^{fl/+}$ and *Fli1*$^{fl/+}$ mice appeared normal and healthy at birth. Germline transmission of the targeted alleles was confirmed. *Ewsr1*$^{fl/+}$ and *Fli1*$^{fl/+}$ mice were crossed to obtain mice having both mutations.

Genomic chromosomal translocation between chromosomes 9 and 11 in the *Ewsr1*$^{fl/+}$:*Fli1*$^{fl/+}$:*CAG-Cre* (EFCC) mice. The *Ewsr1*$^{fl/+}$ and *Fli1*$^{fl/+}$ mice were further crossed with *CAG-Cre*, *Mx1-Cre* or *Rosa26-CreER* mice to induce somatic chromosomal translocation between chromosomes 9 and 11 (Fig. 2A). Dual color fluorescence *in situ* hybridization (FISH) analysis of embryonic fibroblasts derived from the EFCC mice showed juxtaposition of the signal on *der9* of BAC clone RPCI-23 64E17 from chromosome 11 and that of 218O31 from chromosome 9 (Fig. 2B). Reciprocal genomic translocations in systemic organs were examined by genomic PCR using *Ewsr1*- and *Fli1*-specific primers, and both *Ewsr1-Fli1* and *Fli1-Ewsr1* translocations were detected in tail skin of all the mice examined (n = 30). The translocations in systemic organs were examined in three mice, and both *Ewsr1-Fli1* and *Fli1-Ewsr1* translocations were detected in all the organs examined (Fig. 2C). The results indicated that *lox*P-mediated recombination was effective at inducing somatic translocation by ubiquitous *Cre* recombinase expression. The frequencies of the chromosomal translocations were 1.5×10^{-5} at the highest in heart and 1×10^{-6} in bone marrow as estimated by quantitative genomic PCR comparing *Ewsr1-Fli1* and *Trib1* signals (Fig. 2D). The estimated translocation frequencies in the model are higher than those observed in ES cells described in the previous report[3]. When *Cre* recombinase was inducibly expressed by tamoxifen or polyIpolyC administration in a *Rosa26-CreER* or *Mx1-Cre* background, respectively, both *Ewsr1-Fli1* and *Fli1-Ewsr1* translocations were observed (four mice each) (Fig. 2e). However, the translocations

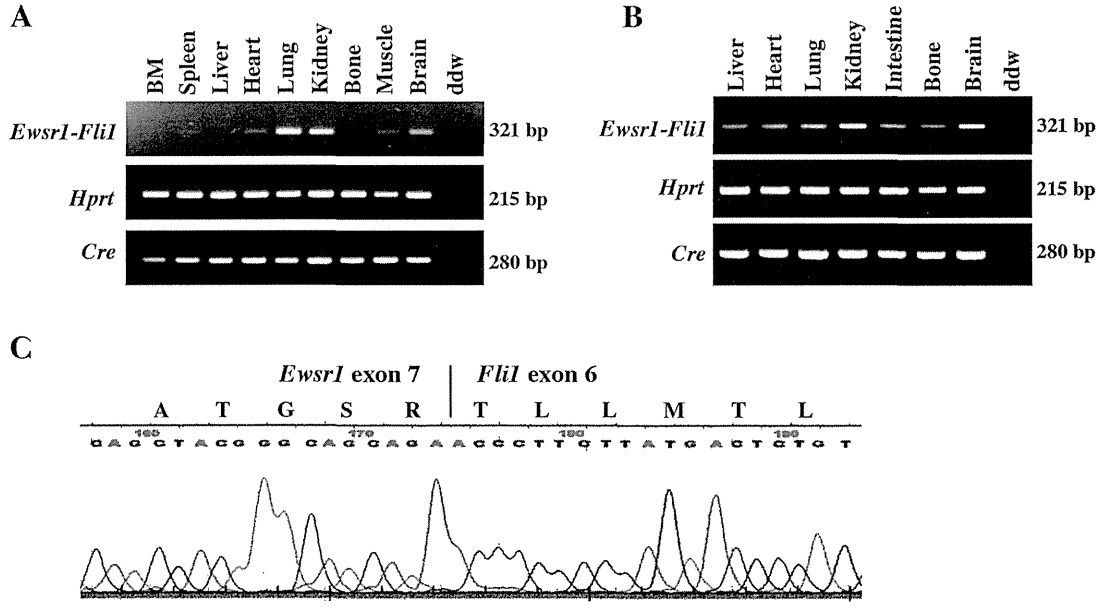

Figure 3 | ***Ewsr1* is fused in-frame to *Fli1*.** (A, B) RT-PCR to detect *Ews-Fli1* fusion transcripts in adult (A) and embryonic tissues (B). Data are representatives of three independent experiments with similar results. (C) Sequence analysis of the RT-PCR product using heart cDNA shows the in-frame fusion between *Ewsr1* exon 7 and *Fli1* exon 6. Deduced amino acid sequences are indicated on the nucleotide sequences.

were detected only by nested PCR in limited organs, indicating that recombination was less frequent in these *Cre* transgenes. In addition, inducible expression of *Cre* upon in the *Mx1-Cre* background resulted in translocations being limited to hematopoietic tissues.

Detection of chimeric *Ewsr1-Fli1* fusion transcripts in EFCC mice. To confirm that gene fusion between *Ewsr1* and *Fli1* was accompanied by the anticipated transcription, RT-PCR was performed using RNA samples obtained from systemic organs of both adult and embryonic mice (three mice each) (Fig. 3A, 3B). The *Ewsr1-Fli1* fusion was detected in all the embryonic organs examined, and the expression of the fusion gene was decreased in bone and liver of the adult mice. Diminished *Ewsr1-Fli1* expression in adult bone and liver might be related to decreased proliferative activity of osteochondrogenic tissues and disappearance of embryonic hematopoietic cells, respectively. No reciprocal *Fli1-Ewsr1* fusion transcript was detected in any of the organs examined (data not shown). The cDNA sequence of the *Ewsr1-Fli1* fusion transcript was analyzed by sequencing, and in-frame fusion between *Ewsr1* exon 7 and *Fli1* exon 6 was confirmed (Fig. 3C). It is expected that the fusion product included both the EWS Q-rich repeats and the FLI1 ETS DNA binding domain[11]. Thus, the data strongly suggested that a functional EWS-FLI1 protein was produced by somatic chromosomal translocation in the model.

EFCC mice died of chronic cardiac failure due to dilated cardiomyopathy. No malignant neoplasms, including Ewing's sarcoma-like lesions, were observed in EFCC mice (n = 30) for a two year period after birth. Neither sarcomas nor benign neoplasms were detect by careful examination of mice irrespective of age. Instead, most of the EFCC mice showed growth retardation and decreased motility. All the EFCC mice died by 100 weeks of age with a mean survival time of only 40 weeks (Fig. 4A). The diseased mice were carefully examined at autopsy and they showed extensive dilatation of heart (Fig. 4B). The heart weight/body weight ratio as well as heart weight itself of EFCC mice was significantly greater than that of control mice from 31 to 42 weeks (Fig 4C, Table 1). Mice of the age were selected since the severity of cardiac lesions was significantly varied in younger EFCC mice. The pathological examination further revealed the cardiac lesions and subsequent systemic congestive changes. The hearts of EFCC mice showed extensive dilatation of both the ventricles and thin ventricular wall without any signs of cardiac hypertrophy (Fig 4D). The earlier the mice became sick, the more severe the cardiac lesions were. High power views of cardiac sections indicated a disorganized arrangement of myocardial fibers with increased collagen fibers between the muscle bundles. The subendocardial area was severely affected and leukocytic infiltration was sometimes present. There was severe chronic congestion in systemic organs such as lung, liver or spleen accompanied by ischemic necrosis around the central vein of the liver (Fig. 4E).

Consistent with the pathological findings, echocardiographic analysis revealed reduced wall thickness, significant fractional shortening and decreased ejection fraction in EFCC mice (Fig. 5, Table 2). In contrast, there was no significant difference in blood pressure, heart rate or diastolic dimension between EFCC and wild-type mice (Table 2). Collectively, these findings are consistent with those of dilated cardiomyopathy.

***Ewsr1-Fli1* translocation and *Ewsr1-Fli1* expression induced myocardial damage.** To obtain insights into the mechanisms of dilated cardiomyopathy in EFCC mice, the cardiac lesion was further investigated. Laser microdissection followed by genomic PCR to detect the *Ewsr1-Fli1* translocation was carried out (Fig. 6A). *Ewsr1-Fli1* was abundantly observed in the outer area of the ventricular wall, however, no signal was detected in the subendocardial area where the myocardial damage was more severe (Fig. 6A, 1 and 3). Severer damages in the subendocardial area were observed in most of mice, though the reason for such uneven distribution of cardiac lesions was unclear. The results suggested degeneration of cardiac myocytes with translocation and perhaps gradual loss due to the pathologic effects of *Ewsr1-Fli1* expression. Indeed, a TUNEL assay using the cardiac sections showed significantly increased apoptosis in EFCC mice compared to wild-type (Fig. 6B).

The toxic effect of *Ewsr1-Fli1* was directly evaluated by its exogenous expression in cultured cardiac myocytes. The murine neonatal cardiac myocytes were infected with *Ewsr1-Fli1*-lentivirus and the frequencies of apoptosis were evaluated (Fig. 6C). The TUNEL assay

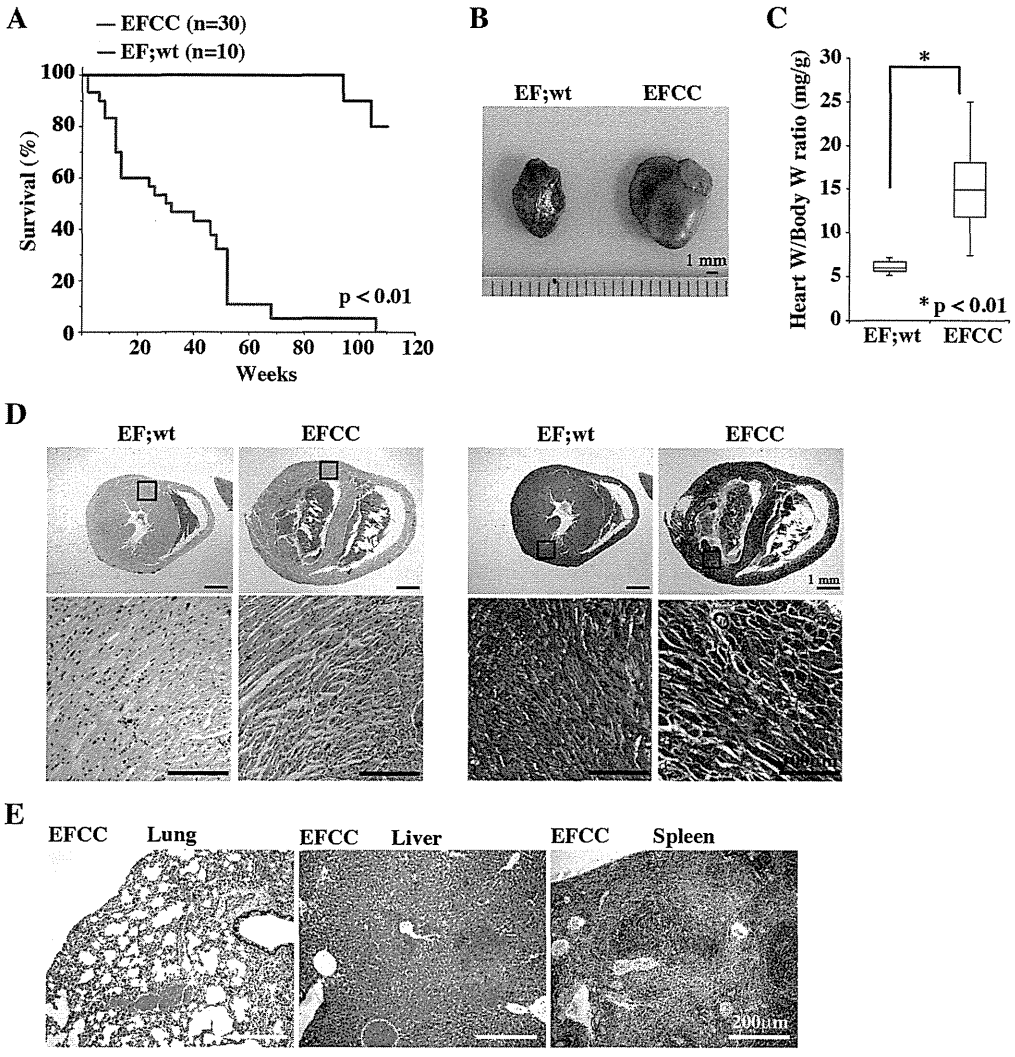

Figure 4 | EFCC mice died of chronic cardiac failure. (A) Kaplan-Meier survival curve. Statistical significance was evaluated by the log-rank test. (B) Cardiac enlargement in the EFCC mouse (right) compared to EF;wild-type (left). (C) Box plot of the heart weight/body weight ratios for EF;wild-type (n = 6) and EFCC mice (n = 6). (D) Extensive ventricular dilatation of the heart in the EFCC mouse without myocardial hypertrophy (top). High power view of myocardium with H&E (middle) and Masson's trichrome staining (bottom). Extensive fibrosis is indicated as blue staining in the EFCC heart. (E) Chronic congestion of systemic organs in EFCC mice including lung, liver and spleen. Note necrotic changes around the central vein of liver.

showed that apoptosis of cardiac myocytes was significantly increased when *Ewsr1-Fli1* was expressed in the cardiac myocytes. The Annexin V/PI flow cytometry analysis showed increases of both early and late apoptosis as well as necrosis in cardiac myocytes by *Ewsr1-Fli1* expression (Fig. 6C). These results indicated that *Ewsr1-Fli1* induced cellular apoptosis in the cardiac tissue, resulting in cellular damage and eventual dilated cardiomyopathy. In addition, *Ewsr1-Fli1* expression in human cardiac fibroblasts induced increased expression of *COL1A1* (Fig. 6D), suggesting that *Ewsr1-Fli1* may also play some role in cardiac fibrosis.

A previous study indicated that the high level of expression of Cre recombinase itself showed cardiac toxicity[12]. The expression level of the Cre protein in the hearts of the EFCC mouse was therefore compared with high-expressing *Cre* transgenic mice (Fig. 6E). *Cre* expression of EFCC mice was comparable to the low *Cre* transgenic mice that did not show cardiac lesions. The results indicated that the cardiac lesion was caused not by *Cre* expression but by *Ewsr1-Fli1*.

Discussion

Cre/*lox*P-mediated chromosomal translocations in mouse models have been reported[5,13,14]. In those studies *lox*P sites were inserted into the introns of *Mll* or *Af9* genes, and the mice carrying the mutations were crossed to place *lox*P sites in both genes. Both ubiquitous and hematopoietic-specific expression of Cre recombinase induced *in vivo* chromosomal translocation and the fusion of *Mll* and *Af9*, resulting in leukemia development. In contrast, leukemia was not observed in the mice bearing chromosomal translocation between *AML1* and *ETO in vivo* using a similar protocol[15].

In the present study, *Ewsr1-Fli1* fusion was successfully induced in various organs. Ewing's sarcoma, however, did not develop in the mice, suggesting that the cell-of-origin of Ewing's sarcoma might constitute a rare cellular population unlike hematopoietic neoplasms. Supporting this idea, we have recently succeeded in developing Ewing's sarcoma-like small round cell tumors by introducing *Ews-Fli1* or *Ews-Erg* into eSZ cells that are enriched in embryonic chondrogenic progenitors[16]. Therefore, when chromosomal translocation between *Ewsr1* and *Fli1* is efficiently induced in eSZ cells, Ewing's sarcoma can develop in a certain cohort using the current translocation model. It is likely that ubiquitous *Cre* expression affects most cell lineages both in developing and adult mouse tissues including the true cell-of-origin of Ewing's sarcoma. However, the low frequency of chromosomal recombination could

Table 1 | Heart and body weight of EF;wt and EFCC mice

EF;wt			
Weeks	HW (mg)	BW (g)	HW (mg)/BW (g)
31	180	25.25	7.13
36	140	27.50	5.09
36	140	25.38	5.52
38	210	34.58	6.07
38	180	26.15	6.88
40	150	25.66	5.85
EFCC			
Weeks	HW (mg)	BW (g)	HW (mg)/BW (g)
30	360	19.63	18.34
35	640	25.47	25.12
36	320	25.66	12.47
36	260	22.49	11.56
40	410	23.66	17.33
42	120	16.22	7.40

not induce detectable translocations in such a rare cell type. Perhaps eSZ cell-specific *Cre* expression may enable the induction of Ewing's sarcoma by somatic *Ewsr1* and *Fli1* translocation, and efficient *Cre* expression in the specific spatiotemporal manner in the eSZ cell may be achieved using the promoter/enhancer elements of *Gdf5* or *Erg* genes[17,18].

Expression of *Ews-Fli1* in the majority of primary cells induced cellular apoptosis or senescence[19–21]. Activation of the *Casp3* promoter by EWS-FLI1 was reported, and the activation of caspase 3-dependent signals may be responsible for apoptotic processes in mouse embryonic fibroblasts (MEFs) with ectopic *Ews-Fli1* expression[21]. Indeed, *Ews-Fli1* expression in cardiac myocytes induced apoptotic cell death, though activation of caspase 3 was not detected in cardiac myocytes unlike in MEFs (data not shown). Thus, the low capacity for cardiac myocyte regeneration after birth could not support cardiac homeostasis. This limitation, therefore, could result in gradual but irreversible cardiac damage. In support of this idea, the *Ews-Fli1* fusion was not detected in the severely degenerated area but remained in relatively normal parts of the heart in EFCC mice. Moreover, introduction of *Ews-Fli1* cDNA significantly induced apoptosis in primary cardiac myocytes, indicating the cardiac toxicity of the fusion gene. The cell type-specific epigenetic status may modulate growth inhibitory and tumorigenic activities of EWS-FLI1. Indeed, different chromatin modification was observed between Ewing's sarcoma-sensitive eSZ and –resistant eGP cells[16]. It is noted that wild-type FLI1 protein represses *Col1a1* expression, inhibiting cardiac fibrosis[22]. Interestingly, EWS-FLI1 enhanced *COL1A1* expression in human cardiac fibroblasts, suggesting that it might accelerate fibrotic processes in cardiomyopathy.

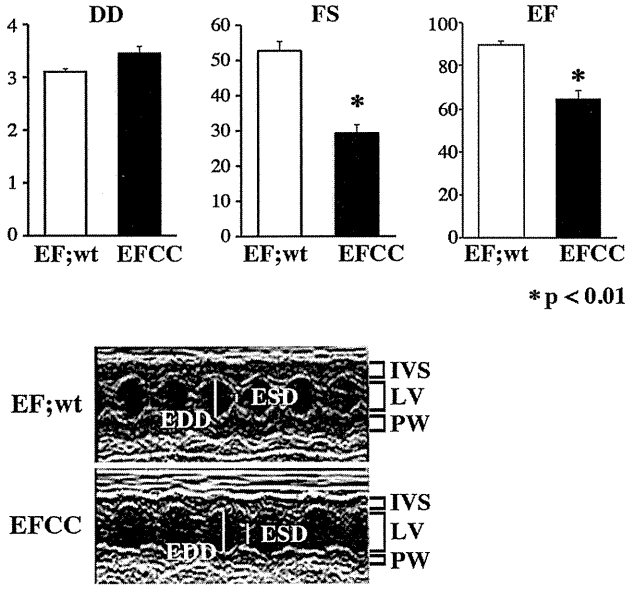

Figure 5 | Echocardiographic analysis of 37-week-old EFCC and EF;wild-type mice. Analysis of cardiovascular function (top). DD, diastolic diameter of left ventricle; FS, fractional shortening; EF, ejection fraction. Representative echocardiogram for wild-type and EFCC mice (bottom). EDD, end-diastolic diameter; ESD, end-systolic diameter, IVS, interventricular septum; LV, left ventricle; PW, posterior wall.

A number of transcription factors are associated with the development and maintenance of cardiac myocytes, and mutations in these factors affect cardiac homeostasis, structure and functions[23]. Over-expression of *E2F6* activates gene expression in myocardium and induces dilated cardiomyopathy in mice[24]. Moreover, mutations in *NKX2-5* and *PDRM16* were found associated with human congenital dilated cardiomyopathy[25,26]. It has been proposed that these proteins regulate genes involved in the ubiquitin proteasome system or proliferation of cardiomyocytes, suggesting different aspects of myocardial damage from the present model. Nevertheless, similar phenotypes shown in these models indicate the importance of cardiac-specific transcriptional regulation by transcription factors, given the low regenerative activity of adult cardiomyocytes.

Methods

Mice and gene targeting. The *Ewsr1* and *Fli1* targeting vectors were assembled in a pBSKSTKLoxPNeoGFP plasmid containing appropriate *lox*P sites, a *lox*P-flanked thymidine kinase (*Tk*) promoter-driven *neo* gene and a *Tk* promoter-driven diphtheria toxin gene. A *Gfp* gene was inserted immediately downstream of the 3′ *lox*P site for the *Ewsr1* vector. The homologous regions of the *Ewsr1* vector consisted of an 8.4 kb genomic fragment containing *Ewsr1* exons 5 to 7 and a 1.3 kb flanking exon 8 (Fig. 1a). Similarly, the *Fli1* vector included a 5.4 kb genomic fragment of *Fli1* intron 5 and a 2.0 kb fragment flanking exon 6. A CMV promoter sequence was also inserted immediately upstream of the 5′ *lox*P site of the *Fli1* vector. To establish mice carrying a single *lox*P allele of *Ewsr1* or *Fli1* genes, the linearized targeting vectors were electroporated into E14 ES cells, and drug-resistant colonies were screened for homologous recombination. To remove the *lox*P-flanked neomycin-resistant gene cassette, the pMCCreGKPuro vector was electroporated into the ES cells, and puromycin-resistant colonies were selected. Targeted clones were injected into C57BL/6 blastocysts and the resultant chimeric mice were bred to produce progeny having germ line transmission of the mutated allele. Mice harboring a targeted *Ewsr1* allele ($Ewsr1^{fl/+}$) and a targeted *Fli1* allele ($Fli1^{fl/+}$) were crossed to establish the mice that possessed *lox*P sites both in *Ewsr1* intron 7 and in *Fli1* intron 5. The resultant

Table 2 | Echocardiographic and hemodynamic analysis

	E/F; wt (n=3)	EFCC (n=4)
Echocardiographic data		
LVDd (mm)	3.01 ± 0.06	3.45 ± 0.13
LVDs (mm)	1.43 ± 0.07	2.43 ± 0.14
IVST (mm)	1.07 ± 0.03	0.78 ± 0.08
LVPWT (MM) **	1.06 ± 0.01	0.76 ± 0.04
FS (%)*	52.67 ± 2.67	29.25 ± 2.43
EF (%)*	89.67 ± 1.67	64.75 ± 3.75
Hemodynamic data		
HR (bpm)	580.7 ± 36.7	631.5 ± 11.9
sBP (mm Hg)	104.3 ± 3.8	105.5 ± 1.4
dBP (mm Hg)	57.7 ± 7.4	50.8 ± 4.5

Values are means ± SEM. LVDd, left ventricular end-diastolic dimension; LVDs, LV end-systolic dimension; IVST, interventricular septum thickness; LVPWT, left ventricular posterior wall thickness; FS, fractional shorting; EF, ejection fraction; HR, heart rate; sBP, systolic blood pressure; dBP, diastolic blood pressure; *, $p < 0.01$; **, $p < 0.05$.

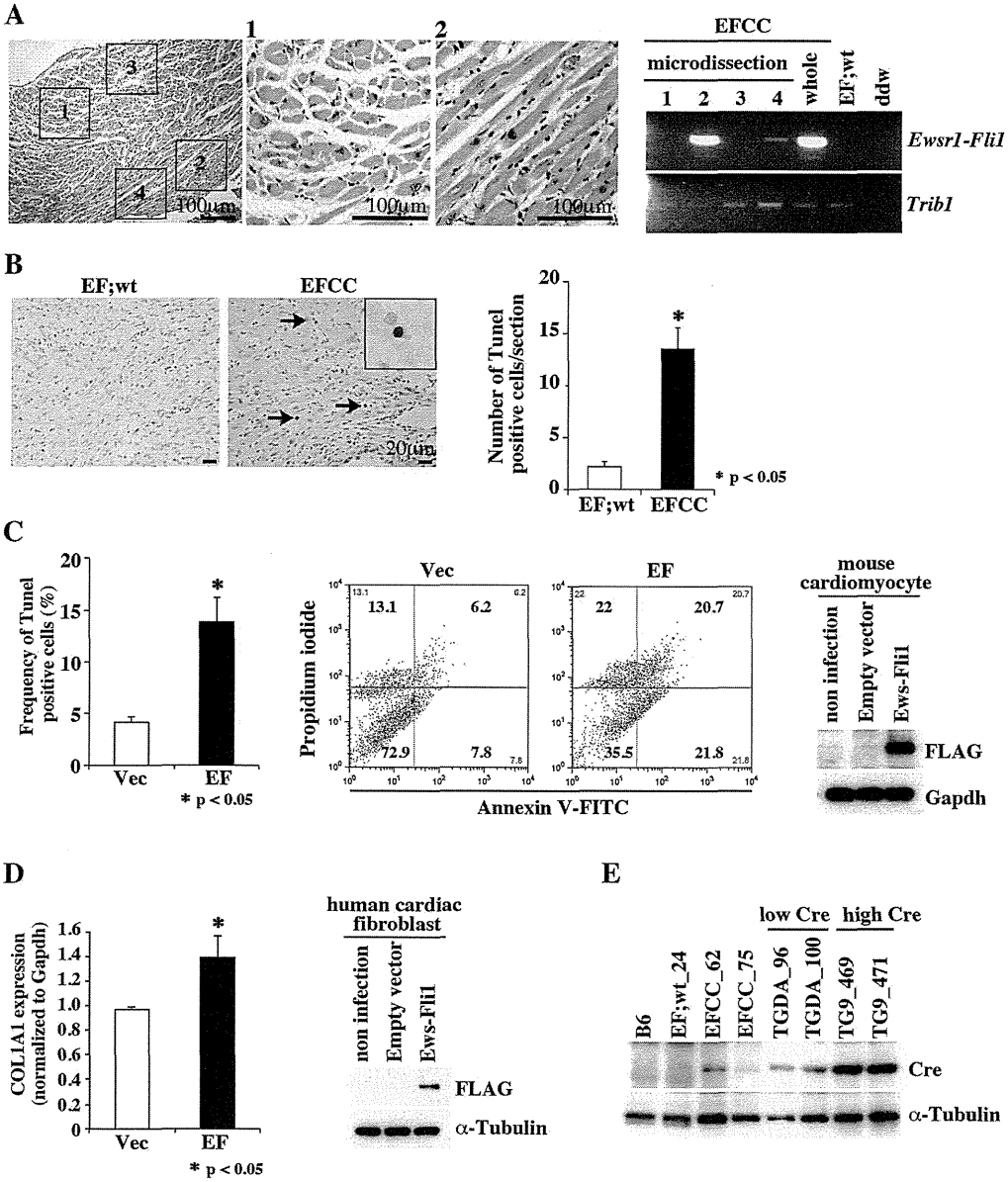

Figure 6 | The cardiac lesion in the EFCC mouse and *Ewsr1-Fli1* translocation. (A) Detection of *Ewsr1-Fli1* translocation in the myocardium. The frozen section of the cardiac tissue from the EFCC mouse was laser microdissected for the indicated areas (1-4) (left). Genomic PCR using DNA samples obtained by laser microdissection (right). (B) A TUNEL assay showed a significantly greater increase of apoptotic cell death in the myocardium of the EFCC mouse than in that of the wild-type mouse (left). High power view of the apoptotic cell is shown in the magnified inset. Frequencies of TUNEL-positive cells per section are compared between wild type and EFCC mice (right). (C) *Ewsr1-Fli1* cDNA expression induced apoptotic cell death of cardiac myocytes *in vitro*. The apoptotic cells were measured by positive signals in a TUNEL assay (left). Ewsr1-Fli1-induced cell death was further analyzed by Annexin V/PI staining and FACS analysis. The lower right quadrant (Annexin V+/PI-) represents early apoptosis, while the upper right quadrant (Annexin V+/PI+) and the upper left quadrant (Annexin V-/PI+) represent late apoptosis and necrosis, respectively. Data are representatives of three independent experiments with similar results (center). The expression of EWS-FLI1 protein in cardiac myocytes was detected by Western blotting using anti-FLAG M2 antibody (right). (D) Quantitative real-time RT-PCR for COL1A1 in human cardiac fibroblasts with or without Ewsr1-Fli1 (left). Expression of EWS-FLI1 protein was detected by Western blotting using anti-FLAG M2 antibody (right). (E) Expression of the Cre protein in the heart of EFCC mice and other *Cre* transgenic lines of variable expression levels[12].

Ewsr1$^{fl/+}$ and *Fli1*$^{fl/+}$ mice were further crossed with *CAG-Cre*, *Mx1-Cre* or *Rosa26-CreER* mice[27–29]. Genotyping of the mice was performed using primers described below. Animals were handled in accordance with the guidelines of the animal care committee at the Japanese Foundation for Cancer Research, which gave ethical approval for these studies.

Southern blotting. Southern blotting was carried out using standard procedures[30]. Genomic DNA samples were digested with *Xba*I or *Sac*I and probed with genomic DNA fragments derived from *Ewsr1* or *Fli1* loci (Fig. 1a).

Fluorescence *in situ* hybridization (FISH). The BAC clones, RPCI-23 64E17 downstream from *Ewsr1* on mouse chromosome 11 and RPCI-23 218O31 upstream from *Fli1* on chromosome 9 were purchased from Invitrogen (Carlsbad, CA) for FISH analysis. The FISH analysis using metaphase spreads obtained from embryonic fibroblasts of the *Ewsr1*$^{fl/+}$:*Fli1*$^{fl/+}$:*CAG-Cre* (EFCC) mouse was performed according to the methods previously described[31].

Genomic and reverse transcription-polymerase chain reaction (gPCR and RT-PCR). Genomic DNA (100 ng) was subjected to 35 cycles of PCR amplification. The

PCR primers to detect the *Ewsr1-Fli1* fusions were as follows. For *Ewsr1-Fli1, Ewsr1* forward primer 5′-ccccagtgcttatccttacatttg-3′ and *Fli1* reverse primer 5′-cctgacccgtgtctttgtag-3′, and for *Fli1-Ewsr1, Fli1* forward primer 5′-agagaacccactgcttactgg-3′ and Ewsr1 reverse primer 5′-accacgccctccaggttcac-3′ were used. To detect the rare translocation in *Rosa26-CreER* and *Mx1-Cre* transgenic mice, genomic DNA samples were pre-amplified using 35 cycles of PCR using the following primers. For *Ewsr1,* the 5′ primer was 5′-ccaagtaggggctctgtcag-3′ and for *Fli1,* the 3′ primer was 5′-ggagctgaagcagtaggaag-3′. For *Fli1,* the 5′ primer was 5′-gccccattgacgcaaatggg-3′ and for Ewsr1, the 3′ primer was 5′-ggggtacttggtgaaggtgc-3′. Genomic PCR for the wild-type *Ewsr1* transgene, Cre recombinase or *Trib1* was performed using the following primers: *Ewsr1,* forward, 5′-cccagtgcttatccttacatttg-3′ and GFP, reverse, 5′-accacgccctccaggttcac-3′, Cre, forward, 5′-catacctggaaaatgcttctgtcc-3′ and Cre, reverse, 5′-attgctgtcacttggtcgtggc-3′, or *Trib1,* forward, 5′-cagtctctccttccaagtcatc-3′ and *Trib1,* reverse, 5′-gattgttgctgctgttgttc-3′. The PCR products were analyzed by 2% agarose gel electrophoresis.

RT-PCR was carried out using cDNA generated from total RNA of systemic organs as previously described[32]. The *Ewsr1-Fli1* fusion transcript was amplified using *Ewsr1* exon 7 primer (5′-tcctcttcacagccgac-3′) and *Fli1* exon 6 primer (5′-ctgctcagtgttcttgcc-3′). The primers for Cre recombinase (forward, 5′-cggtctggcagtaaaaactat-3′; reverse, 5′-cagggtgttataagcaatccc-3′) and *Hprt* (forward, 5′-gctggtgaaaaggacctct-3′; reverse, 5′-cacaggactagaacacctgc-3′) were also used. The PCR products were purified, subcloned into a plasmid and sequenced. Real-time quantitative RT-PCR was performed by using a Fast Real-Time PCR System (Applied Biosystems, Foster City, CA). The primers for human *COL1A1* (forward, 5′-catgaccgagacgtgtggaa-3′; reverse, 5′-tttcttggtcggtgggtgac-3′) and GAPDH (forward, 5′-acctgacctgccgtctagaa-3′; reverse, 5′-aaagtggtcgttgagggcaa-3′) were used.

Echocardiography. Transthoracic echocardiography was performed on conscious, gently restrained mice using a 15-MHz linear probe (Power-Vision 8000, Toshiba, Tokyo, Japan), as described previously[33]. Parasternal long-axis view and short axis view of the left ventricle at the level of the papillary muscles were obtained. 2D-guided M-mode recordings were obtained from short axis view at the level of the papillary muscles. Measurements of interventricular septum thickness (IVST) and left ventricular posterior wall thickness (LVPWT) were made from M-mode recordings in diastole. Left ventricular internal diameter at end-diastole (LVDd) and end-systole (LVDs) were measured from M-mode recordings. Fractional shortening (FS) was calculated as 100 × [(LVDd − LVDs)/LVDd] (%). Ejection fraction (EF) was calculated using the Teichholtz method.

Cell culture and recombinant lentivirus infection. Primary neonatal ICR mouse ventricular myocytes were purchased from Cosmo Bio (Tokyo, Japan), and cells were cultured with D-MEM/F-12 medium supplemented 10% fetal bovine serum (HyClone, South Logan, UT). Human cardiac fibroblasts were purchased from PromoCell (Heidelberg, Germany), and cells were cultured with Fibroblast Medium (ScienCell, Carlsbad, CA). The human *EWSR1-FLI1* cDNA (a kind gift from Susanne Baker) was FLAG-tagged and inserted into the pLVSIN-CMV-neo plasmid (Takara Bio, Tokyo, Japan) and HEK 293 cells were transfected with the plasmid using Lipofectamine 2000 (Invitrogen). Cells were harvested 48 h after lentiviral infection and subjected to further analyses.

TUNEL assay and Annexin-V analysis. Formaldehyde-fixed and paraffin-embedded cardiac tissue sections or methanol-fixed murine primary cardiac myocytes were subjected to TUNEL assays using the DeadEnd Colorimetric TUNEL System (Promega, Madison, WI) according to the manufacturer's protocol. For the Annexin V analysis cells were stained with Annexin V-FITC and propidium iodide (PI) according to the manufacturer's instruction (BD Bioscience Pharmingen, San Diego, CA). The stained cells were immediately evaluated using a FACSCalibur flow cytometer (BD Biosciences, Franklin Lakes, NJ).

Western blotting. Western blotting was performed as previously described[32]. A monoclonal anti-FLAG M2 antibody was purchased from Sigma (St Louis, MO), anti-Cre from Chemicon (Temecula, CA), anti-α-tubulin from Sigma and anti-GAPDH from HyTest (Turku, Finland).

Statistical analysis. Results are shown as means ± standard errors of the mean (SEM). Continuous distributions were compared with two-tailed Student's *t*-tests. Survival analysis was performed using the Kaplan-Meier life table method, and the survival between groups was compared with the log-rank test. All *P* values were two-sided, and a *P* value of less than 0.05 was considered significant.

1. Mitelman, F., Johansson, B. & Mertens, F. The impact of translocation and gene fusions on cancer causation. *Nat. Rev. Cancer* **7**, 233–245 (2007).
2. Taylor, B. S. *et al.* Advances in sarcoma genomics and new therapeutic targets. *Nat. Rev. Cancer* **11**, 541–557 (2011).
3. Smith, A. J. H. *et al.* A site-directed chromosomal translocation induced in embryonic stem cells by Cre-*lox*P recombination. *Nat. Genet.* **9**, 376–385 (1995).
4. Van Deursen, J., Fornerod, M., van Rees, B. & Grosveld, G. Cre-mediated site-specific translocation between nonhomologous mouse chromosomes. *Proc. Natl. Acad. Sci. USA* **92**, 7376–7380 (1995).
5. Forster, A. *et al.* Engineering de novo reciprocal chromosomal translocations associated with *Mll* to replicate primary events of human cancer. *Cancer Cell* **3**, 449–458 (2003).
6. Delattre, O. *et al.* Gene fusion with an *ETS* DNA-binding domain caused by chromosome translocation in human tumours. *Nature* **359**, 162–165 (1992).
7. Sorensen, P. H. *et al.* A second Ewing's sarcoma translocation, t(21;22), fuses the EWS gene to another ETS-family transcription factor, ERG. *Nat. Genet.* **6**, 146–151 (1994).
8. Ordonez, J. L., Osuna, D., Herrero, D., de Alava, E. & Madoz-Gurpide, J. Advances in Ewing's sarcoma research: where are we now and what lies ahead? *Cancer Res.* **69**, 7140–7150 (2009).
9. Torchia, E. C., Boyd, K., Rehg, J. E., Qu, C. & Baker, S. J. *EWS/FLI-1* induces rapid onset of myeloid/erythroid leukemia in mice. *Mol. Cell. Biol.* **27**, 7918–7934 (2007).
10. Zucman, J. *et al.* Combinatorial generation of variable fusion proteins in the Ewing family of tumours. *EMBO J.* **12**, 4481–4487 (1993).
11. Riggi, N., Cironi, L., Suva, M. L. & Stamenkovic, I. Sarcomas: genetics, signaling, and cellular origins. Part I: The fellowship of TET. *J. Pathol.* **213**, 4–20 (2007).
12. Buerger, A. *et al.* Dilated cardiomyopathy resulting from high-level myocardial expression of Cre-recombinase. *J. Card. Fail.* **12**, 392–398 (2006).
13. Collins, E. C., Pannell, R., Simpson, E. M., Forster, A. & Rabbitts, T. H. Inter-chromosomal recombination of *Mll* and *Af9* genes mediated by cre-*loxP* in mouse development. *EMBO Rep.* **1**, 127–132 (2000).
14. Drynan, L. F. *et al.* *Mll* fusions generated by Cre-*loxP*-mediated *de novo* translocations can induce lineage reasignment in tumorigenesis. *EMBO J.* **24**, 3136–3146 (2005).
15. Buchholz, F., Regaeli, Y., Trumpp, A. & Bishop, J. M. Inducible chromosomal translocation of *AML1* and *ETO* genes through Cre/loxP-mediated recombination in the mouse. *EMBO Rep.* **11**, 133–139 (2000).
16. Tanaka, M. *et al.* Ewing's sarcoma precursors are highly enriched in embryonic osteochondrogenic progenitors. *J. Clin. Invest.* **121**, 3061–3074 (2014).
17. Storm, E. E. & Kingsley, D. M. GDF5 coordinates bone and joint formation during digit development. *Dev. Biol.* **209**, 11–27 (1999).
18. Vijayaraj, P. *et al.* Erg is a crucial regulator of endocardial-mesenchymal transformation during cardiac valve morphogenesis. *Development* **139**, 3973–3985 (2012).
19. Deneen, B. & Denny, C. T. Loss of p16 pathways stabilizes EWS/FLI1 expression and complements EWS/FLI1 mediated transformation. *Oncogene* **20**, 6731–6741 (2001).
20. Lessnick, S. L., Dacwag, C. S. & Golub, T. R. The Ewing's sarcoma oncoprotein EWS/FLI induces a p53-dependent growth arrest in primary human fibroblasts. *Cancer Cell* **1**, 393–401 (2002).
21. Sohn, E. J. *et al.* EWS/FLI1 oncogene activates caspase 3 transcription and triggers apoptosis *in vivo*. *Cancer Res.* **70**, 1154–1163 (2010).
22. Elkareh, J. *et al.* Marinobufagenin induces increases in procollagen expression in a process involving protein kinase C and Fli-1: implications for uremic cardiomyopathy. *Am. J. Physiol. Renal. Physiol.* **296**, F1219–F1226 (2009).
23. Oka, T., Xu, J. & Molkentin, J. D. Re-employment of developmental transcription factors in adult heart disease. *Semin. Cell Dev. Biol.* **18**, 117–131 (2007).
24. Westendorp, B. *et al.* The E2F6 repressor activates gene expression in myocardium resulting in dilated cardiomyopathy. *FASEB J.* **26**, 2569–2579 (2012).
25. Costa, M. W. *et al.* Functional characterization of a novel mutation in *NKX2-5* associated with congenital heart disease and adult-onset cardiomyopathy. *Circ. Cardiovasc. Genet.* **6**, 238–247 (2013).
26. Arndt, A. K. *et al.* Fine mapping of the 1p36 deletion syndrome identifies mutation of *PRDM16* as a cause of cardiomyopathy. *Am. J. Hum. Genet.* **93**, 67–77 (2013).
27. Sakai, K. & Miyasaki, J. A transgenic mouse line that retains Cre recombinase activity in mature oocytes irrespective of the cre transgene transmission. *Biochem. Biophys. Res. Commun.* **237**, 318–324 (1997).
28. Kuhn, R., Schwenk, F., Aguet, M. & Rajewsky, K. Inducible gene targeting in mice. *Science* **269**, 1427–1429 (1995).
29. Ventura, A. *et al.* Restoration of p53 function leads to tumour regression *in vivo*. *Nature* **445**, 661–665 (2007).
30. Iwasaki, M. *et al.* Identification of cooperative genes for NUP98-HOXA9 in myeloid leukemogenesis using a mouse model. *Blood* **105**, 784–793 (2005).
31. Kawamura-Saito, M. *et al.* Fusion between CIC and DUX4 up-regulates PEA3 family genes in Ewing-like sarcomas with t(4;19)(q35;q13) translocation. *Hum. Mol. Genet.* **15**, 2125–2137 (2006).
32. Nakamura, T. *et al.* Evi9 encodes a novel zinc finger protein that interacts with BCL6, a known human B-cell proto-oncogene. *Mol. Cell. Biol.* **20**, 3178–3186 (2009).
33. Kuwahara, K. *et al.* NRSF regulates the fetal cardiac gene program and maintains normal cardiac structure and function. *EMBO J.* **22**, 6310–6321 (2003).

Acknowledgments

We are grateful to Junichi Miyazaki for CAG-Cre, Klaus Rajewsky for MX1-Cre and Tyler Jacks for Rosa26-Cre transgenic mice. We also thank Miki Yamazaki, Yohei Kanno, Hitomi Yamanaka and Tokuichi Kawaguchi for technical assistance. This work was supported by

the Grants-in-Aid for Scientific Research from the Ministry of Education, Culture, Sports, Science and Technology (23791672 and 26250029) to M.T. and T.Na.

Author contributions

M.T., T.No. and T.Na. designed the work. M.T., S.Y., Y.Y. and H.K. performed the experiments. M.T., K.K., K.N., P.Y.J., T.No. and T.Na. analyzed the data. M.T. and T.Na. wrote the paper. All co-authors contributed in the form of discussion and critical comments.

Additional information

Competing financial interests: The authors declare no competing financial interests.

How to cite this article: Tanaka, M. *et al.* Somatic chromosomal translocation between *Ewsr1* and *Fli1* loci leads to dilated cardiomyopathy in a mouse model. *Sci. Rep.* **5**, 7826; DOI:10.1038/srep07826 (2015).

Journal of Molecular and Cellular Cardiology 80 (2015) 81–89

Contents lists available at ScienceDirect

Journal of Molecular and Cellular Cardiology

journal homepage: www.elsevier.com/locate/yjmcc

Original article

Ectopic automaticity induced in ventricular myocytes by transgenic overexpression of HCN2

Kensuke Oshita [a,b], Masayuki Itoh [a], Shingo Hirashima [c], Yoshihiro Kuwabara [d], Keiko Ishihara [a], Koichiro Kuwahara [d], Kazuwa Nakao [e,f], Takeshi Kimura [d], Kei-ichiro Nakamura [c], Kazuo Ushijima [b], Makoto Takano [a,*]

[a] Department of Physiology, Kurume University School of Medicine, Kurume, Japan
[b] Department of Anesthesiology, Kurume University School of Medicine, Kurume, Japan
[c] Division of Microscopic and Developmental Anatomy, Department of Anatomy, Kurume University School of Medicine, Kurume, Japan
[d] Department of Cardiovascular Medicine, Graduate School of Medicine, Kyoto University, Kyoto, Japan
[e] Medical Innovation Center, Graduate School of Medicine, Kyoto University, Kyoto, Japan
[f] Department of Medicine and Clinical Science, Graduate School of Medicine, Kyoto University, Kyoto, Japan

ARTICLE INFO

Article history:
Received 16 July 2014
Received in revised form 5 December 2014
Accepted 22 December 2014
Available online 3 January 2015

Keywords:
HCN2
Arrhythmia
Ion channel
Cardiomyocyte
Electrophysiology

ABSTRACT

Hyperpolarization-activated cyclic nucleotide-gated channels (HCNs) are expressed in the ventricles of fetal hearts but are normally down-regulated as development progresses. In the hypertrophied heart, however, these channels are re-expressed and generate a hyperpolarization-activated, nonselective cation current (I_h), which evidence suggests may increase susceptibility to arrhythmia. To test this hypothesis, we generated and analyzed transgenic mice overexpressing HCN2 specifically in their hearts (HCN2-Tg). Under physiological conditions, HCN2-Tg mice exhibited no discernible abnormalities. After the application of isoproterenol (ISO), however, ECG recordings from HCN2-Tg mice showed intermittent atrioventricular dissociation followed by idioventricular rhythm. Consistent with this observation, 0.3 μmol/L ISO-induced spontaneous action potentials (SAPs) in 76% of HCN2-Tg ventricular myocytes. In the remaining 24%, ISO significantly depolarized the resting membrane potential (RMP), and the late repolarization phase of evoked action potentials (APs) was significantly longer than in WT myocytes. Analysis of membrane currents revealed that these differences are attributable to the I_h tail current. These findings suggest HCN2 channel activity reduces the repolarization reserve of the ventricular action potential and increases ectopic automaticity under pathological conditions such as excessive β-adrenergic stimulation.

1. Introduction

Hyperpolarization-activated cyclic nucleotide-gated channels (HCNs) are widely expressed in a variety of tissues [1]. Among the four HCN subtypes (HCN1-4), HCN2 and HCN4 are abundantly expressed in the pacemaker cells of the sinoatrial node, where they generate a hyperpolarization-activated, nonselective cation current (I_f/I_h), which plays a key role in cardiac pacemaker activity [2]. HCN2 and 4 are also expressed in ventricular myocytes early during fetal development but are down-regulated at later stages [3,4].

As many as 50% of patients with heart failure die from sudden cardiac death, most likely caused by a lethal arrhythmia [5]. In heart failure and cardiac hypertrophy, the cardiac remodeling process reactivates ventricular myocardial expression of such fetal cardiac genes as HCN2 and HCN4 as well as CACNA1G and CACNA1H, which encode T-type Ca^{2+} channel subunits [6–8]. Although the mechanisms responsible for lethal arrhythmias in failing hearts remain unresolved, evidence suggests re-expression of fetal type cardiac ion channels contributes to the arrhythmogenicity. Indeed, when we generated transgenic mice that selectively expressed a dominant-negative neuron-restrictive silencer factor mutant in their hearts (dnNRSF-Tg mice), we found that these mice experienced sudden arrhythmic death and that there was a concomitant up-regulation of fetal type cardiac ion channels [9]. However, the contribution of each fetal cardiac channel to the arrhythmogenicity remains uncertain.

We previously reported that pharmacological blockade of HCN channels partially suppressed sudden arrhythmic death in dnNRSF-Tg mice [9]. We also carried out a preliminary analysis of transgenic mice overexpressing HCN2 in their hearts (HCN2-Tg) and reported that they were vulnerable to β-adrenergic-induced abnormal electrical activity [10]. In the present study, we carried out a detailed analysis of

* Corresponding author at: Department of Physiology, Kurume University School of Medicine, 67 Asahi-machi, Kurume 830-0011, Japan. Tel.: +81 942 31 7543; fax: +81 942 31 7728.
E-mail address: takanom@med.kurume-u.ac.jp (M. Takano).

http://dx.doi.org/10.1016/j.yjmcc.2014.12.019

the electrocardiographic and electrophysiological properties of single ventricular myocytes from HCN2-Tg mice. Our findings demonstrate that HCN2 channel activity reduces the repolarization reserve of the ventricular action potential (AP) and increases the ectopic automaticity of ventricular myocytes.

Preliminary results from this study were communicated at the annual meeting of the Japanese Physiological Society (Tokyo 2013) and at the Congress of the International Union of the Physiological Society (Birmingham 2013) [11].

2. Materials and methods

All animal experiments were approved in advance by the Animal Ethics Committee of Kurume University (No. 23-11). Animal care and experiments conform to the Guidelines for the Care and Use of Laboratory Animals published by the US National Institutes of Health (NIH Publication No. 85-23, revised 1996).

2.1. Experimental animals

We overexpressed mouse HCN2 cDNA in the hearts of C57BL/6 mice using the α-MHC promoter (HCN2-Tg) [10]. HCN2-Tg and their wild-type (WT) littermates were used while they were between 10 and 14 weeks of age.

2.2. Cell isolation

After deeply anesthetizing mice using 3.0% sevoflurane, their hearts were quickly removed and the ventricular myocytes were isolated through collagenase digestion [12].

2.3. Heterologous expression experiment

Mouse HCN2 cDNA was subcloned into pCDNA3 vector, which was then transfected into CHO cells using Attractene (QIAGEN). Electrophysiological studies were carried out 2 days after the transfection.

2.4. Electrophysiological measurements

APs and membrane currents were recorded from ventricular myocytes using ruptured and perforated whole-cell patch clamp methods. The composition of the pipette solutions and the bathing solutions are available in the on-line data supplement. All the experiments were carried out at 33–35 °C.

2.5. Quantitative RT-PCR analysis

Levels of mouse HCN1 (TaqMan assay ID: Mm00468832_m1), HCN2 (Mm00468538_m), HCN3 (Mm01212852_m1), HCN4 (Mm01176086_m1), Kir2.1 (Mm00434616_m1), Cav1.2 (Mm01188822_m1), Kv4.2 (Mm00807577_m1), Kchip2 (Mm00518915_g1) and Kv11.1 (Mm01161732_m1) mRNA were determined using quantitative real-time RT-PCR (qPCR) in predesigned TaqMan Gene Expression Assays (Applied Biosystems, Inc.). Relative levels of mRNA were normalized to the level of 18S rRNA.

2.6. ECG recording

Mice were anesthetized using 2.0% sevoflurane and placed in a supine position on a warming plate to maintain body temperature at around 37 °C. Two-lead ECGs (lead I, lead II) were recorded and analyzed using a PowerLab Data Acquisition System with LabChart software (AD Instruments Inc.). Vector ECGs were reconstructed using lead I and lead aVF. Lead aVF was calculated using following equation:

$$\text{lead aVF} = \frac{1}{\sqrt{3}} \times (2 \times \text{lead II} - \text{lead I})$$

2.7. Fluorescence immunohistochemistry

Mice were anesthetized with 3% sevoflurane and perfused through the left ventricle with heparinized saline followed by 4% paraformaldehyde in PBS. The hearts were removed and post-fixed for 2 h with 4% paraformaldehyde, cryoprotected for 18 h in 30% sucrose, and mounted in OCT Embedding Compound (Sakura Finetek, Japan), after

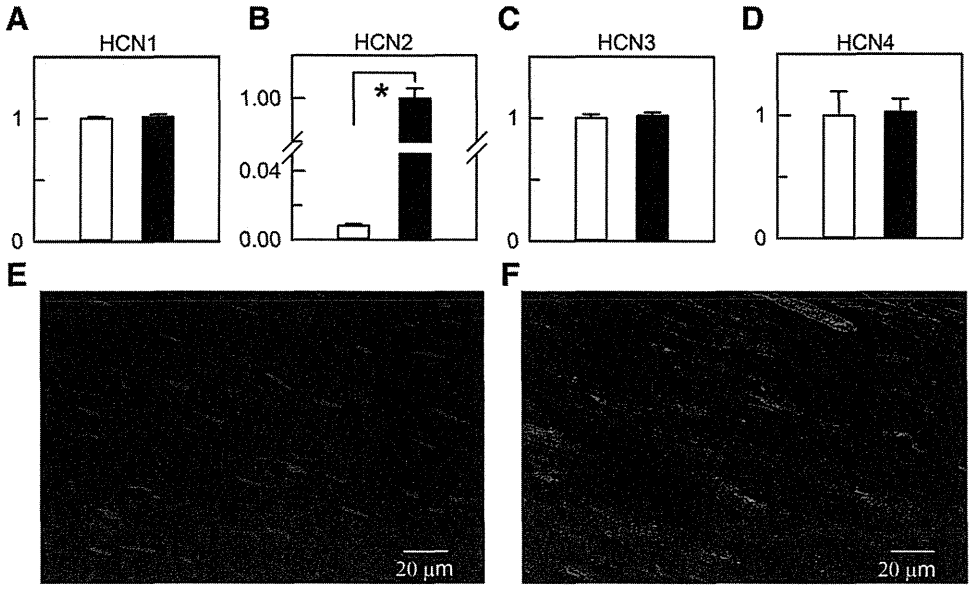

Fig. 1. Expression levels of HCN subtypes in the ventricles of HCN2-Tg mice (A–D) qPCR analysis of the relative mRNA level of HCN family proteins in ventricles from WT (white bars, $n = 5$) and HCN2-Tg (black bars, $n = 5$) mice. Note that the expression level of HCN2 mRNA is significantly higher in HCN2-Tg than WT hearts ($p < 0.01$). (E, F) Immunohistochemical staining for HCN2 demonstrating the subcellular localization of HCN2 in WT (E) and HCN2-Tg (F) ventricles. Nuclei were stained blue with DAPI. Bars represent 20 μm.

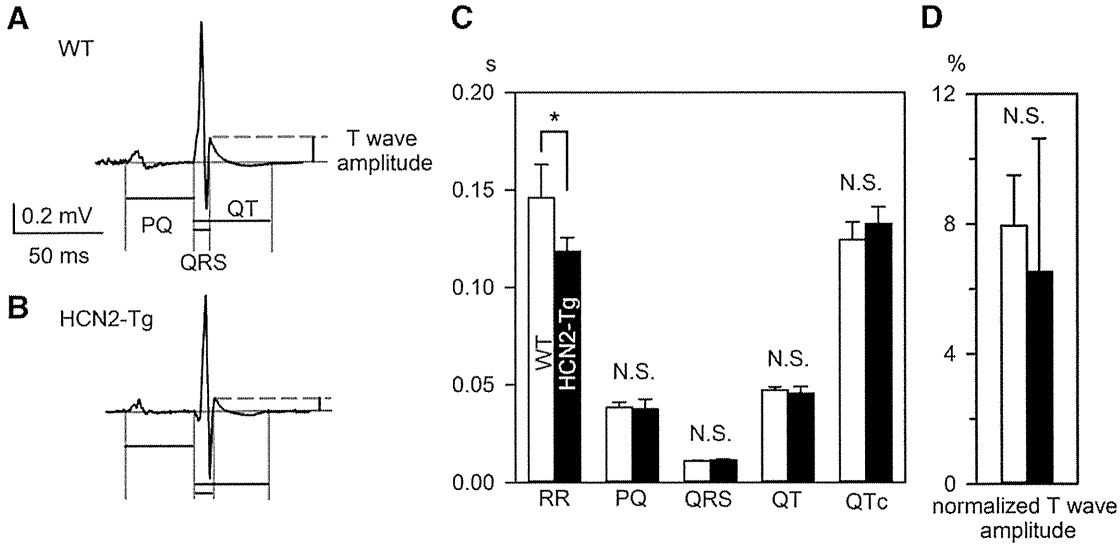

Fig. 2. ECG parameters in WT and HCN2-Tg mice (A, B) Representative ECG traces in WT (A) and HCN2-Tg (B) mice. Definitions of the PQ, QRS and QT intervals and the T-wave amplitude are indicated. (C) ECG parameters in WT (white bars, $n = 5$) and HCN2-Tg (black bars, $n = 5$) mice. In HCN2-Tg mice, RR intervals were significantly shorter than in WT mice. Other parameters (PR interval, QRS interval, QT interval, QTc (Bazett's Formula)) did not significantly differ between WT and HCN2-Tg mice. (D) Relative T-wave amplitudes in WT (white bar) and HCN2-Tg (black bar) mice.

which serial 5-μm sections were cut with a cryostat (CM3050S, Leica Microsystems, Wetzlar, Germany). The tissue sections were washed in PBS and then blocked with 5% normal goat serum (NGS) in PBS containing 0.05% Triton X-100. Thereafter, the sections were incubated with a polyclonal rabbit anti-HCN2 antibody (1:1000 dilution, Alomone Labs, Jerusalem, Israel) for 1 day at 4 °C, followed by incubation with Alexa Fluor 568 goat anti-rabbit IgG (1:2000 dilution, Invitrogen, Carlsbad, CA) for 2 h at room temperature. Images were captured using a Fluoview 1000 laser-scanning confocal microscope system (Olympus, Tokyo, Japan).

2.8. Statistical analysis

Data are shown as mean ± SD. Repeated-measures one-way analysis of variance (ANOVA) followed by the Tukey test and the Student's *t*-

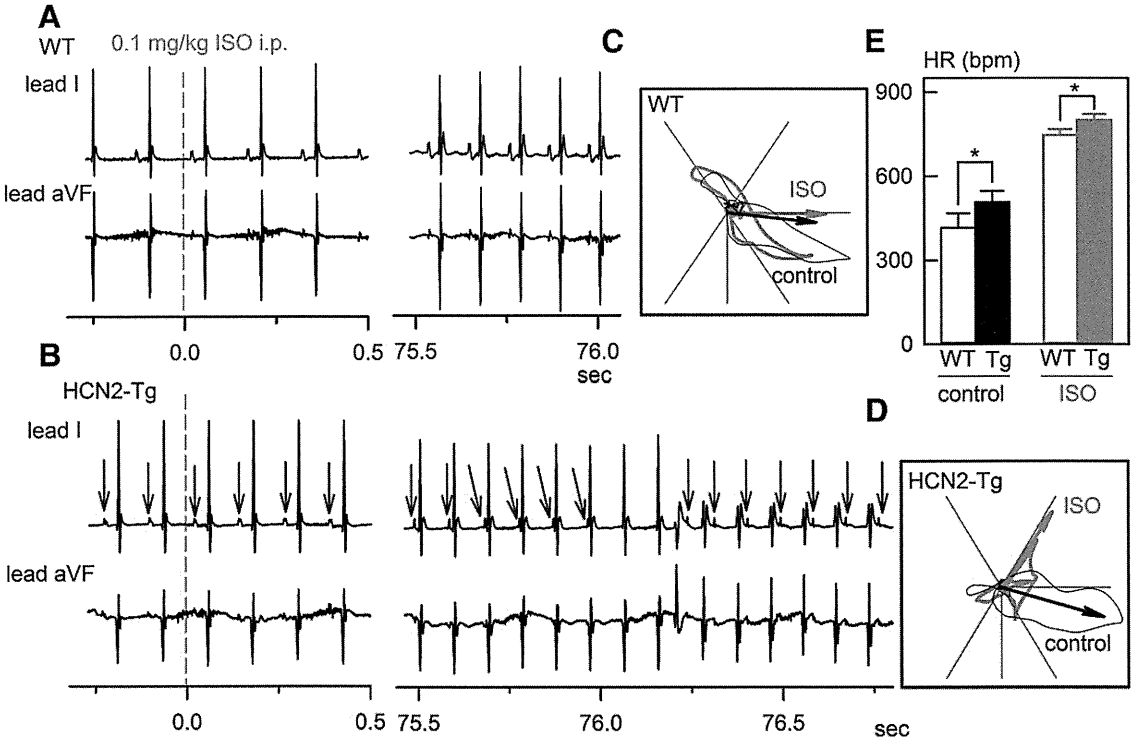

Fig. 3. Idioventricular rhythm induced by ISO in HCN2-Tg mice (A, B) Representative ECG traces in WT (A) and HCN2-Tg (B) mice. Under control conditions, we observed no arrhythmias in WT or HCN2-Tg mice. ISO (0.1 mg/kg) was intraperitoneally injected at 0 s. Note that in HCN2-Tg mice the ECG trace showed atrioventricular dissociation followed by idioventricular rhythm. The blue arrows indicate P waves to emphasize the AV dissociation. (C) Representative vector ECG in WT mice before (black) and after (red) ISO application. (D) Representative vector ECG in HCN2-Tg mice. ISO induced ectopic ventricular rhythm in HCN2-Tg hearts. (E) Heart rates in WT (open bar) and HCN2-Tg (filled bar) mice before (black) and after (red) ISO administration. With or without ISO, heart rates in HCN2-Tg mice were significantly faster than in WT mice.

test were used for data analysis. Differences were considered significant when $p < 0.05$.

3. Results

3.1. Isoproterenol (ISO) induces idioventricular rhythm in HCN2-Tg mice

Recent studies suggest that in addition to HCN2, HCN1 and HCN3 may also be involved in generating murine ventricular APs [13,14]. We therefore first examined whether the expression of these channels was altered in HCN2-Tg myocytes. qPCR experiments showed that there were no secondary changes in the expression of HCN1, HCN3 or HCN4 in HCN2-Tg myocytes. On the other hand, HCN2 expression was >100 times higher in HCN2-Tg than WT myocytes (Figs. 1A–D). Immunostaining confirmed that virtually no HCN2 was present in WT ventricular ventricles. In HCN2-Tg hearts, however, HCN2-immunoreactivity was ubiquitous throughout the ventricle (Fig. 1F).

Free moving, telemetric ECG records from HCN3 knockout mice ($HCN3^{-/-}$) revealed significant changes in the waveform: the QT interval was prolonged at lower heart rates in $HCN3^{-/-}$ mice, and the amplitude of the T-wave was greater [14]. By contrast, the only significant change in the ECG waveform in HCN2-Tg mice was a shortening of the RR interval (Fig. 2). The relative amplitude of the T-wave (normalized to the amplitude of the R-wave) varied considerably, and there was no significant difference between the WT ($7.9 \pm 1.5\%$, $n = 5$) and HCN2-Tg ($6.5 \pm 4.1\%$, $n = 5$, $p = 0.49$) hearts.

We previously reported that β-adrenergic stimulation increased the occurrence of ventricular arrhythmias during telemetric recording of ECGs in HCN2-Tg mice [10]. To explore the mechanism of this arrhythmia, we carried out electrocardiographic vector analysis under general anesthesia [15]. In WT mice, the intraperitoneal application of ISO (0.1 mg/kg) simply induced sinus tachycardia; no ventricular arrhythmias were observed, and the polarity of the QRS complex and the morphology of the vector loop were not significantly changed. By contrast, ISO-induced atrioventricular dissociation in HCN2-Tg mice, followed by idioventricular rhythm (Fig. 3B). These ventricular rhythms occurred intermittently and returned to sinus rhythm when the AV dissociation disappeared. Vector ECG revealed that upward vector loop and left

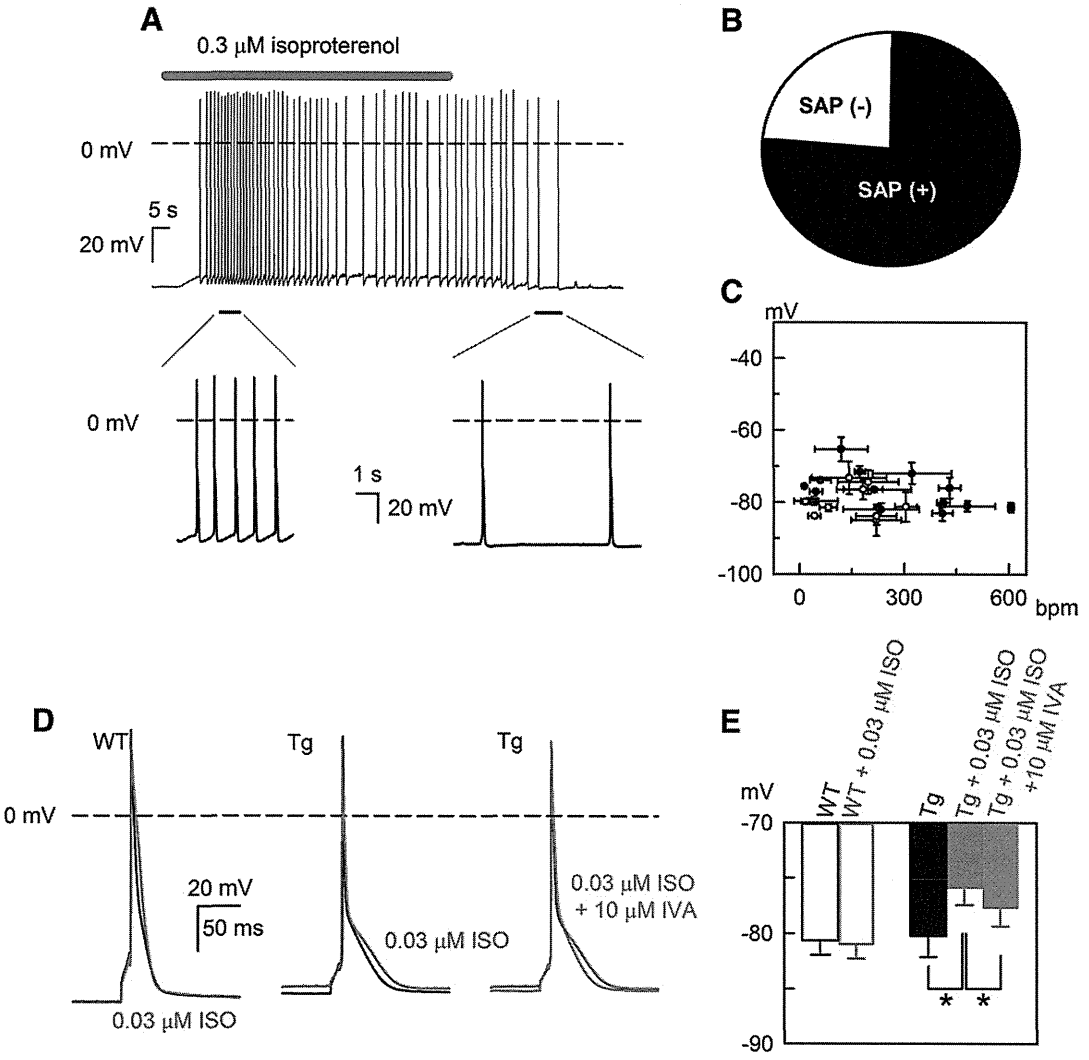

Fig. 4. ISO-induced SAP in HCN2-Tg myocytes (A) Continuous trace of a current-clamp recording from an HCN2-Tg myocyte. In this experiment, the membrane potential was recorded using the perforated patch method. The application of 0.3 μmol/L ISO is indicated by the red bar. (B) Fractions of ISO-treated HCN2-Tg myocytes with and without SAPs. The black sector indicates the percentage of myocytes exhibiting SAPs (76%). (C) Scatter plot of MDPs and firing rates (beats per min; bpm) of SAPs in ISO-treated HCN2-Tg myocytes: white symbols, data recorded using the perforated whole-cell patch method; black symbols, ruptured whole-cell patch method. Firing rates were calculated by successively averaging the inter-AP intervals in trains of SAPs; inter-AP intervals were measured from the onset of SAPs to the termination of ISO application. (D) Representative induced AP waveform in WT (left) and HCN2-Tg (center, right) myocytes. In HCN2-Tg, depolarization of RMP was observed at even lower concentration (0.03 μmol/L ISO). It should be noted that 10 μmol/L ivabradine significantly reversed the depolarization. In WT, ISO (red line) neither induced depolarization of RMP nor SAP. (E) RMPs in WT myocytes (open bars, $n = 6$) and in HCN2-Tg myocytes (filled bars, $n = 10$); control, black bars; with ISO, red bars; with ISO and IVA, green bar (repeated-measures one-way ANOVA followed by Tukey test, $^*p < 0.05$).

axis deviation were consistently induced during the idioventricular rhythm (Fig. 3D). These findings suggest that ISO increased ectopic pacemaker activity in the ventricles of HCN2-Tg hearts (Figs. 3A, C).

3.2. ISO induces depolarization and spontaneous APs in HCN2-Tg myocytes

To obtain insight into the cellular mechanism underlying the ectopic ventricular rhythm in HCN2-Tg mice, we recorded the membrane potentials of HCN2-Tg myocytes using pipette solution containing 5 mmol/L EGTA. As shown in Fig. 4A, the application of 0.3 μmol/L ISO depolarized the resting membrane potential (RMP) and often induced an irreversible train of spontaneous APs (SAPs); i.e., SAPs were observed in 76% of cells tested (32 of 42 cells, Fig. 4B). Fig. 4C summarizes the relationship between the average firing rates and the maximal diastolic potentials (MDPs) of SAPs in HCN2-Tg myocytes. The white symbols depict the values recorded in the perforated whole-cell patch experiments ($n = 9$), while the black symbols represent those recorded in the ruptured whole-cell patch experiments. However, the occurrence of SAPs did not differ between the experimental configurations. Twenty-four percent of ventricular myocytes isolated from HCN2-Tg hearts, ISO depolarized the RMP, but did not induced SAPs (data not shown). It was recently reported that HCN2 channel possessed permeability to Ca^{2+}, as well as Na^+ and K^+, which may induce delayed after depolarization (DAD) [16]. To test this possibility, we carried out fast pacing of HCN2-Tg myocytes. As shown in Supplementary Fig. 1, DAD was not induced both in the presence and absence of ISO, when recorded with 5 mmol/L EGTA pipette solution. These findings suggested that intracellular Ca^{2+}-dependent mechanism may not be involved in this automaticity.

In HCN2-Tg myocytes, ISO depolarized RMP even at lower concentration; 0.03 μmol/L ISO depolarized RMP from -80.2 ± 1.9 mV to -75.9 ± 1.6 mV (Fig. 4E, $n = 10$, $p < 0.05$). The depolarization of RMP was significantly reversed by the application of HCN channel blocker, ivabradine from -75.9 ± 1.6 mV to -77.6 ± 1.7 mV (Fig. 4E, $n = 10$, $p < 0.05$). In WT myocytes, ISO neither induced SAPs (data not shown) nor depolarized the RMP (Fig. 4D, left panel), which were -80.6 ± 1.3 mV and -81.0 ± 1.3 mV in the absence and presence of 0.03 μmol/L ISO, respectively (Fig. 4E, $n = 6$). ISO (0.3 μmol/L) also failed to induce SAP or depolarization in WT myocytes (data not shown).

To clarify the mechanisms underlying ISO-induced depolarization and SAPs, we next evaluated the membrane currents that contribute to the RMP. As shown in the right panel of Fig. 5A, inhibition of I_{K1} using 1 mmol/L Ba^{2+} unmasked a time-dependent inward current activated by hyperpolarizing pulses (i.e., I_h) in HCN2-Tg myocytes. In WT cells, I_h was negligibly small or absent when the K^+ concentration in the bathing solution was within the physiological range (Fig. 5A, left panel). The current–voltage (I–V) relationships for I_h (open circles) and the background current (filled circles) are shown in Fig. 5D.

We also compared the amplitudes of the inward-rectifier K^+ current (I_{K1}) measured as a Ba^{2+}-sensitive component. The I–V relationships in Fig. 5B show that I_{K1} density did not significantly differ between WT (open triangles) and HCN2-Tg (filled triangles) myocytes. Consistent with this observation, qPCR revealed that levels of Kir2.1 mRNA also did not significantly differ between WT and HCN2-Tg myocytes (Fig. 5C).

To determine whether I_h could be activated at membrane potentials close to the MDP or depolarized RMP in HCN2-Tg myocytes, we analyzed voltage-dependent, steady-state I_h activation curves before and after the application of ISO (Fig. 5E). We used a 2-step pulse protocol, in which conditioning pulses (to -50 and to -150 mV for 1250 ms) were followed by a test pulse to -150 mV, as shown in the upper panel of Fig. 5A. The amplitudes of the time-dependent components at the onset of test pulse were normalized as %activation and plotted. We then fitted the Boltzmann equation to each data set: %activation $= 1/(1 + \exp((V_m - V_{1/2}) / s))$, where $V_{1/2}$ is the membrane potential at which activation is half-maximal, V_m is the membrane potential, and s is the slope factor. It is clear from Fig. 5E that $V_{1/2}$ was shifted from -118.5 ± 2.9 mV to -90.2 ± 1.5 mV by ISO application ($n = 4$, $p < 0.01$). These activation curves suggest that under control conditions 7% of I_h is activated at RMP, whereas in the presence of ISO as much as 25% of I_h is activated at the MDP (-77.1 ± 4.7 mV) of SAPs.

Finally, we compared the time course of the diastolic depolarization of SAPs and the activation time course of I_h in HCN2-Tg myocytes (Fig. 5F). As indicated by the dashed lines, the activation kinetics of I_h at -80 mV were so fast that the current could be sufficiently activated

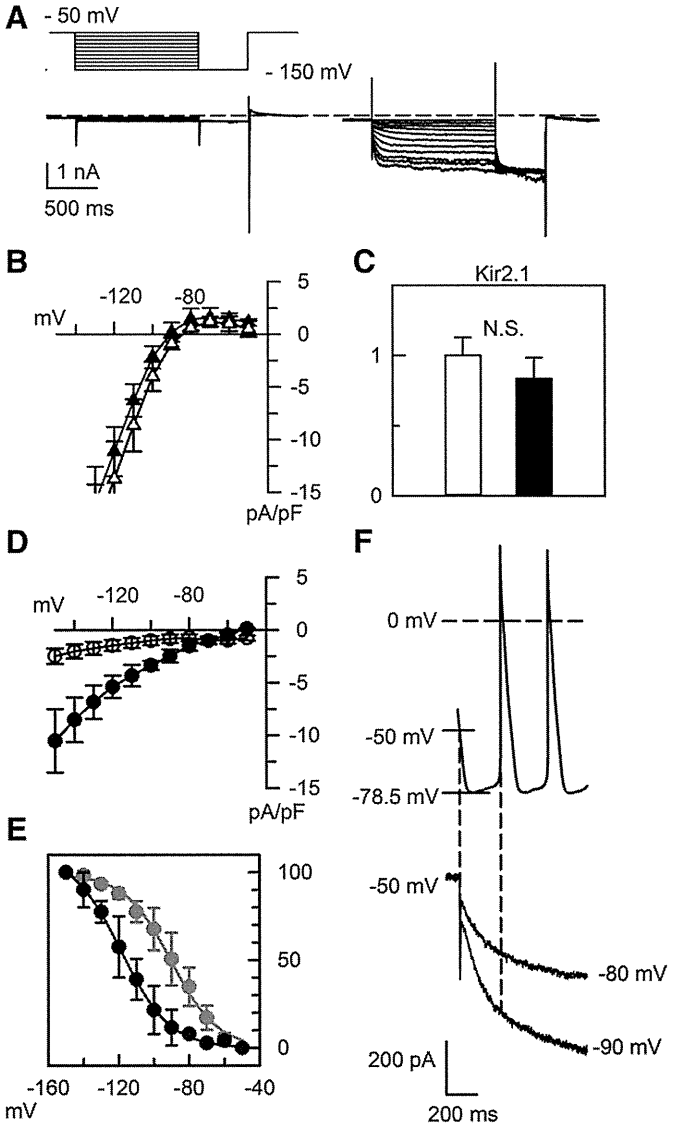

Fig. 5. Shift of the I_h activation curve underlies the depolarization of RMP in HCN2-Tg myocytes. (A) Representative current traces recorded from WT (left) and HCN2-Tg (right) myocytes after the application of 1 mmol/L Ba^{2+}. A robust I_h was revealed after complete inhibition of I_{K1}. The pulse protocol is indicated above the traces. (B) I–V relationship for I_{K1} in WT (open triangles) and HCN2-Tg (filled triangles) myocytes. I_{K1} amplitude was measured as the Ba^{2+}-sensitive component. (C) qPCR analysis of the relative levels of Kir2.1 mRNA in WT (open bar) and HCN2-Tg (filled bar) hearts ($n = 5$ in each group). (D) I–V relationship for I_h in HCN2-Tg myocytes (filled circles) in the presence of 0.3 μmol/L ISO. The amplitude of the time-dependent component during the conditioning pulse was measured as I_h and normalized to the cellular membrane capacitance. In WT myocytes, only the time-independent background current was observed (open circles). (E) Voltage-dependent steady-state activation curve for I_h in the presence (red circles) and absence (black circles) of 0.3 μmol/L ISO. (F) Upper panel shows an expanded SAP trace. The MDP was -78.5 mV, and the peak-to-peak interval was 209 ms. The lower panel shows the time course of I_h activation in HCN2-Tg myocytes at -80 and -90 mV. The membrane current was recorded in bathing solution containing 1 mmol/L Ba^{2+} and 0.3 μmol/L ISO.

at MDP during the beat-to-beat intervals between SAPs. This strongly suggests that in HCN2-Tg myocytes, ISO-induced depolarization of RMP and diastolic depolarization of SAPs are due to ISO-induced activation of HCN2.

3.3. Repolarization reserve in HCN2-Tg myocytes

Fenske et al. [14] recently reported detecting faint expression of HCN3 in ventricular myocytes from adult mice. They also reported that in HCN3 knockout ($HCN3^{-/-}$) mice, AP duration (APD) was shortened along with alteration of T-wave amplitude on ECGs. We therefore used ruptured whole-cell patch methods to evaluate the shape of APs induced in HCN2-Tg myocytes.

In Fig. 6A, AP was recorded in the absence of ISO. The black and red lines indicate APs of WT and HCN2-Tg, respectively. As summarized in Fig. 6C, the amplitude of action potential (APA) was not significantly different between HCN2-Tg and WT myocytes. AP duration at 90% repolarization (APD_{90}) was significantly longer, whereas APD_{50} and APD_{20} were significantly shorter in HCN2-Tg myocytes. Fig. 6B depicts the AP waveforms recorded in the presence of 0.3 μmol/L ISO. APs were induced in the same cells as in Fig. 6A. In HCN2-Tg myocyte, the RMP was depolarized due to the activation of HCN2. At the same time, and the amplitude of overshoot was reduced, most probably due to the inactivation of voltage-gated Na^+ current at depolarized RMP. Action potential parameters are summarized in Fig. 6C; APA was significantly smaller in HCN2-Tg. The differences of APD_{90}, APD_{50}, and APD_{20} were even more apparent in the presence of ISO.

At the given composition of the intra- and extracellular solutions, predicted reversal potential of I_h was −35 mV. During repolarization phase, it is therefore anticipated that outward tail current of I_h shortened APD at the membrane potentials more positive than −35 mV, and inward tail current of I_h prolonged APD at the membrane potentials more negative than −35 mV. To test this idea, we carried out AP clamp experiments in CHO cells expressing mouse HCN2 cDNA. We used CHO cells because they do not express voltage-gated K^+ currents, and it was easy to isolate I_h tail currents from the background current. We first activated I_h using a square pulse protocol with high-K^+ pipette solution containing 1 mmol/L cAMP (Fig. 7A). It should be noted that the direction of the tail current reversed between −40 and −30 mV. When we then perfused 5.4 mmol/L K^+, 10 mmol/L Cs^+ bathing solutions, inward I_h was almost completely blocked, but the outward tail current was less sensitive to this solutions.

In the same cell, we activated I_h using a command pulse shaped like an AP sampled from an HCN2-Tg myocyte in the presence of ISO (Fig. 7B, inset). In the left panel of Fig. 7B, the black line was recorded in the control bathing solution, the green line in the 5.4 mmol/L K^+, 10 mmol/L Cs^+ bathing solution. It is clear that a Cs^+-sensitive component was recorded during all phases of the AP. In the right panel of Fig. 7B, the *I–V* relationship was obtained from the repolarization phase in the AP clamp experiment ($n = 6$). The intersections between black line and magenta line show that the reversal potential of the Cs^+-sensitive component was close to −35 mV. It is evident from these results that the I_h tail current could participate in the repolarization phase of the mouse ventricular AP.

Finally, we confirmed that the expression of ion channels that could potentially affect APD was unchanged in HCN2-Tg myocytes. qPCR analyses showed that the expression of Cav1.2, Kv11.1, Kv4.2 and Kchip2 did not significantly differ between WT and HCN2-Tg myocytes. Furthermore, we detected no secondary changes in the densities of L-type Ca^{2+} currents and 4-AP-sensitive transient outward currents in HCN2-Tg myocytes (Supplementary Fig. 2).

4. Discussion

Evidence from numerous studies is suggestive of the potential arrhythmogenicity of HCNs in failing hearts but much remains unclear. For example, HCN2 and HCN4 are up-regulated in hypertrophied rat hearts and in the human failing heart [8,17,18]. In the mouse transverse aortic constriction (TAC) model, however, the amplitude of I_h is significantly increased, but there is a concomitant up-regulation of only HCN1

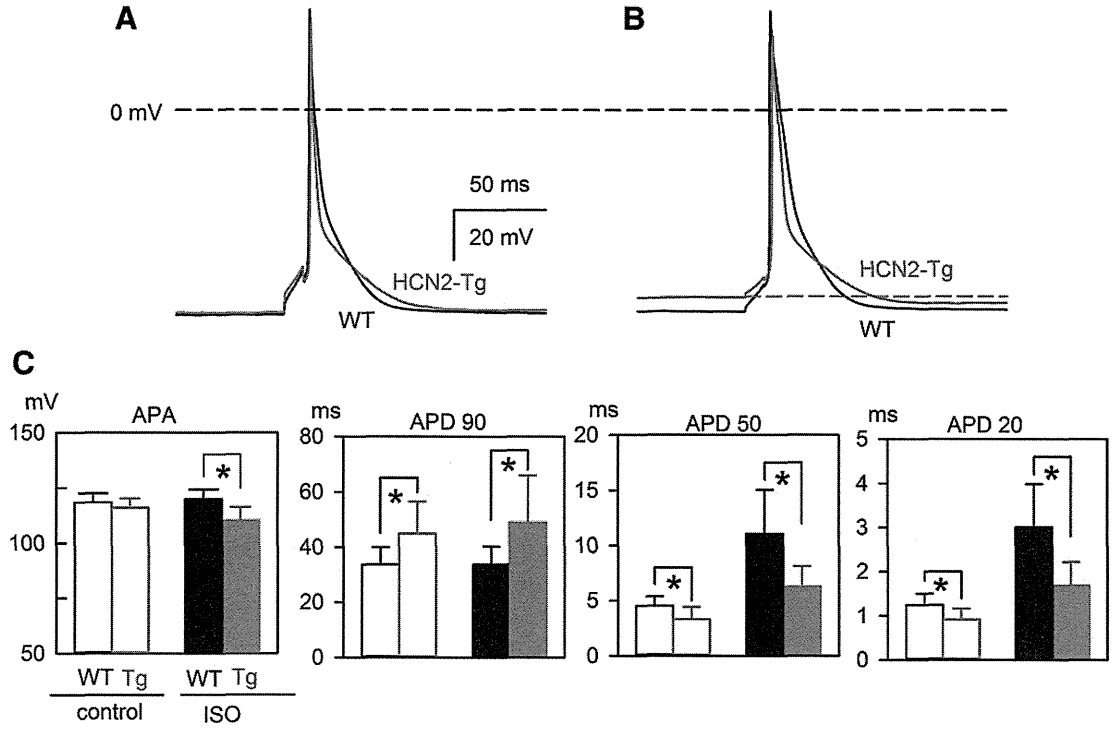

Fig. 6. Action potential parameters of induced APs (A) Representative AP traces of WT (black line) and HCN2-Tg myocyte (red line) under control condition. (B) AP traces in the presence of 0.3 μmol/L ISO. Black and red lines, same as in (A). As emphasized by the red dash line, depolarization of RMP was observed only in HCN2-Tg myocytes. (C) Summaries of APA, APD_{90}, APD_{50}, APD_{20}: black bars, WT; red bars, HCN2-Tg; open bars, without ISO; filled bars, with 0.3 μmol/L ISO. Bars depict means ± S.D., $^*p < 0.05$.